1	
2	
3	
4	
5	
6	
7	
8	Propagation of Radar Rainfall Uncertainties into Urban Pluvial Flood
9	Modeling during the North American Monsoon
10 11 12 13	Annika Hjelmstad ^{(1),(2)} , Ashish Shrestha ⁽¹⁾ , Margaret Garcia ⁽¹⁾ , and Giuseppe Mascaro ⁽¹⁾
14 15	(1) School of Sustainable Engineering and the Built Environment, Arizona State University,
16	Tempe, AZ, USA
17	(2) Department of Civil and Environmental Engineering, Henry Samueli School of
18	Engineering, University of California at Irvine
19	
20	Revised version submitted to:
21 22	Hydrological Sciences Journal
23 24 25 26 27	Corresponding Author: Giuseppe Mascaro, School of Sustainable Engineering and the Built Environment, Arizona State University, ISTB4, Building 75, Room 395C, Tempe, AZ 85281, USA. Email: gmascaro@asu.edu

Abstract

Pluvial flooding in urban regions is a natural hazard that has been rarely investigated. Here, we evaluate the utility of three radar (Stage IV, MRMS, and GCMRMS) quantitative precipitation estimates (QPEs) and the SWMM hydrologic-hydraulic model to simulate pluvial flooding during the North American Monsoon in Phoenix. We focus on an urban catchment of 2.38 km² and, for four storms, we simulate a set of flooding metrics using the original QPEs and an ensemble of 100 QPEs characterizing radar uncertainty through a statistical error model. We find that Stage IV QPEs are the most accurate, while MRMS QPEs are positively biased and their utility to simulate flooding increases with the gage correction done for GCMRMS. For all radar products, simulated flood metrics have lower uncertainty than QPEs as a result of rainfall-runoff transformation. By relying on extensive precipitation and basin datasets, this work provides useful insights for urban flood predictions.

1. Introduction

41

42

43

44

45

46

47

48

49

50

51

52

53

54

55

56

57

58

59

60

61

62

63

Flooding is the most common natural hazard, causing large property losses and fatalities worldwide (Doocy et al., 2013). For example, in the United States (U.S.) major flooding events have caused an annual average of \$9.1 billion in losses and 71 fatalities between 2004-2015 (The National Academies Press, 2019). The impacts of flooding are particularly significant in urban regions, due to population growth concentrated in cities (Cohen, 2006; Hossain et al., 2015); land cover modifications increasing surface imperviousness (W. Zhang et al., 2018); and climate change potentially causing more severe precipitation extremes (Emanuel, 2005; Prein et al., 2017; Trenberth et al., 2003). Urban areas may be impacted by pluvial, fluvial, and coastal flooding. Fluvial flooding results from a river overtopping its banks. Coastal flooding occurs when storm surge or extreme high tides inundate the shore and/or cause inland flooding through the drainage network. Pluvial flooding takes place when runoff exceeds the capacity of natural and built drainage systems to collect water and safely transport it to a receiving water body (Rosenzweig et al., 2018). Here, we focus on urban pluvial flooding, a process that has been rarely systematically measured and modeled while being a significant driver of urban flooding (Rosenzweig et al., 2018; The National Academies Press, 2019). While pluvial flooding is often considered "nuisance" flooding, it can result in building damage, traffic impacts, power outages, and weakened infrastructure (ten Veldhuis, 2011). A key resource to mitigate the impacts of urban flooding is the availability of accurate hydrometeorological forecasts with sufficient lead times. In the U.S. operational flood and flash food forecasts are provided by the National Weather Service (NWS), an agency of the National Oceanic and Atmospheric Administration (NOAA). These forecasts rely on quantitative precipitation estimates (QPEs) and forecasts (QPFs) generated through the integration of weather

radar data, rain gage observations, and numerical weather prediction models. QPEs and QPFs are used as forcings for the Sacramento Soil Moisture Accounting (SAC-SMA) hydrologic model (Z. Zhang et al., 2012), which produces flood forecasts at ~3,600 locations across the nation (Salas et al., 2018). Flash flood guidance values are also generated in certain regions of the country (D. Seo et al., 2013). NWS River Forecast Centers (RFCs) and Weather Forecast Offices (WFOs) use these different sources of hydrometeorological forecasts to issue flood and flash flood watches and warnings to inform the public on the potential occurrence and danger of these events (NOAA, 2020). For urban regions where catchments have small response times and no streams, flood and flash flood watches and warnings are often based solely on QPEs, QPFs, and expert knowledge of the area.

Despite the low annual precipitation depths, urban pluvial flooding is of significant concern also in desert cities (Saber et al., 2020; Thakali et al., 2016). These include the Phoenix metropolitan region in southwestern U.S., which experiences localized convective thunderstorms with high rain rates during the North American Monsoon (NAM) summer season (Adams & Comrie, 1997) resulting in floods and flash floods (Yang et al., 2017, 2019). Due to the combined effect of increasing urbanization and concentration of population, economic activities and infrastructure, pluvial flooding events in the Phoenix metropolitan area have been increasingly impacting transportation, electricity delivery, and properties (NOAA, 2021). Unfortunately, operational forecasts of floods and flash floods driven by NAM convective storms are challenged by the limited ability to (i) predict the exact location, timing and rain rates of convective storms with adequate lead time (Li et al., 2003; Rogers et al., 2017) and (ii) simulate rainfall-runoff processes in urban catchments with highly heterogeneous surface properties and presence of stormwater infrastructure (Leandro et al., 2016).

In this study, we contribute towards the improvement of the predictability and modeling of urban pluvial flooding caused by NAM convective thunderstorms through two main activities. First, we quantify the uncertainty of three radar-based QPE products in the Phoenix metropolitan area during the NAM season (July to October of years 2015-2019). This is a necessary preliminary step to validate and improve both OPEs and OPFs used for hydrologic predictions. The QPEs include the National Centers for Environmental Prediction (NCEP) Stage IV analysis (Y. Lin, 2020), the Multi-Radar Multi-Sensor (MRMS) and its gage corrected version (GCMRMS) system products (J. Zhang et al., 2011, 2016). They all rely on observations of Sband weather radars of the Next Generation Weather Radar (NEXRAD) network that are merged with other data sources that depend on the product. Radar-derived rainfall estimates are affected by errors in (i) reflectivity measurements, (ii) relations converting reflectivity into rainfall rate, and (iii) geometry of the radar measurement field (Villarini and Krajewski, 2010). Although the integration of other data sources and gage observations in radar QPEs limits these errors, their effect can still be significant, especially at hourly and sub-hourly resolutions (Nelson et al., 2016). Here, we characterize the uncertainty of these errors using the multiplicative error model proposed by Ciach, Krajewski, and Villarini (2007). While error models of radar-derived QPEs have been applied in humid (Habib et al., 2008; Villarini & Krajewski, 2009, 2010b) and mountainous regions (Germann et al., 2009; Kirstetter et al., 2010), their application has been limited in arid sites and, to our knowledge, they have never been tested in the desert southwestern U.S. Moreover, to calibrate the error model, we use observations of 168 rain gages in an area of 5,930 km², resulting in one of the largest densities of ground observations used to apply these statistical models.

87

88

89

90

91

92

93

94

95

96

97

98

99

100

101

102

103

104

105

106

107

108

The second main activity of this study is to set up a hydrologic-hydraulic model in an urban catchment in Phoenix and use it to assess the propagation of uncertainty of the QPE products into urban flooding predictions. Simulating urban pluvial flooding in detail is a complex task that requires (i) identifying and collecting data on small-scale spatial heterogeneities of catchment features (e.g., roads and buildings) and stormwater infrastructure; and (ii) incorporating these features in a numerical model that simulates rainfall-runoff processes, surface overland flow, and pipe flow. Progress has been made during the last decade to address some of the major challenges of urban hydrologic modeling (e.g., Chen et al., 2009; Cristiano et al., 2017; Grimley et al., 2020; Leandro et al., 2016; S. Zhang & Pan, 2014). However, current operational hydrologic forecasts by the NWS still rely on models that do not explicitly simulate urban hydrologic and hydraulic processes. Here, we take advantage of the availability of highresolution (0.25 m) terrain from Light Detection and Ranging (LiDAR) and a detailed infrastructure database provided by the City of Phoenix to explore the utility of the EPA Storm Water Management Model (SWMM) model (Koustas, 2000; Rossman, 2010), which is widely adopted for engineering design. After setting up both the 1-D and 2-D versions of SWMM in a basin of 2.38 km², we select four storm events and conduct rainfall-runoff simulations using (i) gage rainfall observations; (ii) Stage IV, MRMS, and GCMRMS QPEs; and (iii) an ensemble of rainfall fields generated with the error model that characterizes the uncertainty of radar-derived QPEs. In doing so, this study focuses on a source of uncertainty (precipitation) affecting urban flood modeling that has received less attention compared to other sources, such as topographic data and parameter specification (e.g., Abily et al., 2016, Deletic et al., 2012). This work provides valuable support for local flood management and forecasting agencies, as well as to improve the recently launched NOAA National Water Model (NWM; NOAA, 2016), which

109

110

111

112

113

114

115

116

117

118

119

120

121

122

123

124

125

126

127

128

129

130

131

relies on MRMS QPEs and a distributed hydrologic model to simulate streamflow at ~2.7 million river locations over the continental U.S. at different lead times.

2. Study Area

The metropolitan area of Phoenix, Arizona (Fig. 1a) is one of the fastest growing urban regions in U.S., with a population that has risen from 1.86 million in 1985 to over 4.75 million in 2018 (Guan et al., 2020). It is located in the southwestern U.S. in a region with a hot desert climate (BWh, according to the Köppen classification) where the mean annual rainfall and temperature are 204 mm and 24 °C, respectively (Mascaro, 2017). The rainfall regime is characterized by marked seasonality, including (1) a summer season from July to September, when the NAM leads to diurnally-modulated convective thunderstorms with high rainfall intensities, very short durations (<1 h) and small spatial extents (Balling & Brazel, 1987), and (2) a dry period from late fall to early summer which is interrupted by occasional cold fronts leading to widespread storm systems with low-to-moderate rainfall intensity and relatively longer durations of up to a few days (Sheppard et al., 2002). The spatial variability of annual, seasonal, and extreme rainfall is moderately to significantly controlled by terrain, which varies from 220 to 2,325 m above mean sea level (Mascaro, 2017, 2018, 2020).

While floods and flash floods occur both in summer and winter in this urban area, pluvial flooding events caused by monsoonal thunderstorms occur more frequently than other types of flood events (Yang et al. 2017; their Fig. 4) and are particularly impactful in small urban catchments with short response times. To investigate the predictability of these events, we simulate urban flooding with different radar rainfall products in an urban catchment of 2.38 km² in downtown Phoenix (Fig. 1b). The basin is largely (~80%) impervious and includes the dense downtown business district, the Phoenix City Hall, and entertainment venues such as the Citi

Field Baseball stadium. As detailed in Fig. 1b, the drainage infrastructure in the catchment includes 657 catch basins, 386 manholes and other junctions, and 1,091 pipe segments totaling 24 km, all draining to one outlet that discharges to the Salt River south of downtown Phoenix. In addition to this surface discharge, there are 26 drywells which capture and infiltrate stormwater.

3. Datasets

155

156

157

158

159

160

161

162

163

164

165

166

167

168

169

170

171

172

173

174

175

3.1. Rainfall Products

We use three radar-derived QPEs, including Stage IV, MRMS and GCMRMS. Stage IV QPEs are produced by processing and mosaicking reflectivity data from the NEXRAD network; rainfall rates are further adjusted with gage and satellite observations and manually quality controlled (Y. Lin, 2020). MRMS products are derived by integrating radar observations from the NEXRAD and Canadian networks, with atmospheric environmental data, satellite data, and lightning and rain gage observations (J. Zhang et al., 2016). We acquire Stage IV and MRMS QPEs for summers (July to October) of 2015-2019. For MRMS, we obtain version 11 of the radar-only and gage-corrected (GCMRMS) products. Stage IV (MRMS; GCMRMS) QPEs are available in polar stereographic coordinates at 4-km, 1-h (1-km, 2-min; 1-km, 1-h) resolution. We project all radar products into Universal Transverse Mercator (UTM) Zone 12N and aggregate MRMS at 1-hour time resolution. To quantify errors in the QPEs and apply the multiplicative error model, we use rainfall records of 168 gages of the Automated Local Evaluation in Real Time (ALERT) network managed by the Flood Control District of the Maricopa County (FCDMC; Fig. 1a). For these tipping-bucket gages, we convert the tipping instants into rainfall intensities at 1-hour resolution following the procedure described by Mascaro et al. (2013).

176

3.2. Geospatial Datasets for Hydrologic-Hydraulic Simulations

We set up the EPA SWMM hydrologic-hydraulic model in the study basin using several geospatial datasets. We use the terrain description from a LiDAR product at an equivalent resolution of 0.25 m that is publicly available (ASU, 2018); soils data from the Natural Resources Conservation Service Web Soil Survey (NRCS, 2019); and percent imperviousness from 30-m map from the National Land Cover Database (MRLC, 2016). We obtain information on drainage infrastructure components from the City of Phoenix, including location of pipes, dry wells, and manholes; pipe material, diameter, and slope; and elevations of pipe rim and invert.

4. Methods

In the following sections, we first describe the statistical error model used to characterize the uncertainty of radar errors and, then, we illustrate the setup of the hydrologic-hydraulic model. Lastly, we detail the approach used to sample the radar rainfall error model to force the hydrologic-hydraulic model and describe the metrics adopted to quantify the associated uncertainty.

4.1. Radar Rainfall Error Model

We use a multiplicative model to characterize the radar rainfall model uncertainty. This type of model has been shown to outperform additive models in terms of predictive skill and ability to separate systematic and random errors, and capture the non-linear relationship between the magnitude of errors and measurement (Tang et al., 2015; Tian et al., 2013). Specifically, we use the model proposed by Ciach, Krajewski, and Villarini (2007) and recently improved by Villarini et al. (2014), who suggested the use of a mixture of gamma distributions instead of the Gaussian distribution to characterize positive multiplicative errors, along with techniques to account for the spatiotemporal structure of the errors. Since the errors of radar-derived products

are affected by the distance from the radar, we divide the rain gages into two clusters, as shown in Fig. 1a, and apply the model separately on each cluster. In the following, we provide a brief description of the model and refer the reader to Ciach, Krajewski, and Villarini (2007) and Villarini et al. (2014) for a detailed description. We also point out that a recent study by Ciach and Gebremichael (2020) has proposed an alternative parametrization of the error model based on a three-parameter modified Laplace model.

The model assumes that the difference between area-averaged radar rainfall estimates and point gage measurements is negligible. In a previous model application in Oklahoma by Ciach et al. (2007), this assumption was supported referring to Ciach and Krajewski (2006), who calculated the spatial correlogram of 1-h rainfall time series observed at pairs of gages with distances, d, lower than 4 km. These authors found the Pearson's correlation coefficient, ρ , to be larger than 0.88, thus suggesting the rainfall spatial variability to be small within a radar pixel. We perform a similar analysis with our dataset by computing the Kendall's τ correlation coefficient to better measure the correspondence between samples that are not well described by the Gaussian distribution (Serinaldi, 2008; Villarini et al., 2014). We then derive ρ from τ using the formula $\rho = sin(\frac{\pi\tau}{2})$ (Fang et al., 2002) and fit the power-law relation:

$$\rho(d) = \rho_0 \exp\left(-\frac{d}{d_0}\right),\tag{1}$$

with parameters ρ_0 and d_0 , to capture the average behavior. We find ρ to be larger than 0.88 for $d \le 1$ km (the MRMS grid resolution), which is similar to the value of Ciach and Krajewski (2006). The minimum ρ decreases instead to 0.72 for d = 4 km, suggesting that a single rain gage may not fully capture the rainfall variability within a Stage IV pixel. Dai et al. (2018) showed that this can introduce uncertainty in the application of a different error model. Since a similar

study has not been yet conducted for the model adopted here and is out the scope of this paper, we will still assume that rain gages provide a relatively accurate estimate of the area rainfall.

According to the multiplicative structure of the error model, the true rainfall value in a radar pixel, R_{true} , can be expressed as the product of a deterministic, $h(R_r)$, and a random, $e(R_r)$, component:

$$R_{true} = h(R_r) \cdot e(R_r). \tag{2}$$

Both functions in equation (2) depend on R_r , which is the radar rainfall value corrected for unconditional bias (if present), computed as:

$$R_r = B_0 \cdot R_r^*. \tag{3}$$

 B_0 is in turn calculated as:

225

226

227

242

243

244

245

$$B_0 = \frac{\sum_i R_{g,i}}{\sum_i R_{r,i}^*},\tag{4}$$

- where $R_{g,i}$ is the rain gage measurement at the *i*-th gage, and $R_{r,i}^*$ is the biased radar rainfall in the co-located pixel (i.e., the original Stage IV, MRMS and GCMRMS values).
- In equation (2), the function $h(R_r)$ provides an estimate of the bias conditioned on R_r ,
 while $e(R_r)$ accounts for residual errors after removing unconditional and conditional biases. We
 obtain the two components as follows. We use rain gage observations, R_g , to approximate R_{true} ;
 next, following Ciach, Krajewski, and Villarini (2007), we compute $h(R_r)$ by (i) applying the
 Epanechnikov kernel with a minimum of 20 data points, and (ii) fitting the power relation:

$$h(R_r) = aR_r^b, (5)$$

with parameters a and b, to the line derived from the kernel. Equation (5) allows obtaining the sample of errors as the ratio of R_g (approximating R_{true}) and $h(R_r)$. We use this sample to find the best parametric distribution to statistically model the random component $e(R_r)$, testing different mixtures of gamma distributions, as proposed by Villarini et al. (2014). For each

distribution, we evaluate the possibility of using parameters that are constant or dependent on R_r and choose the most appropriate one through the Akaike Information Criterion (AIC; Akaike, 1974).

We also test whether the random errors in our dataset exhibit significant spatial and temporal dependencies. For each cluster, we compute the spatial correlogram of the random errors using the Kendall's τ correlation coefficient and the same power model of equation (1), where $\rho(d)$ and ρ_0 are now replaced by $\tau(d)$ and τ_0 , respectively (Fig. S2). We find the nugget parameter τ_0 to range from 0.23 to 0.37 depending on the radar product, thus indicating that the correspondence between errors at close pixels is rather low (Fig. S2). To further verify this assumption, we (i) generate 100 spatially correlated error fields following Villarini et al. (2014), as well as 100 random error fields; and (ii) compute for each field the basin mean areal rainfall during four selected storms (see section 4.3). We find the uncertainties of the basin mean areal rainfall derived from spatially correlated and uncorrelated fields to be very similar (not shown). To quantify the temporal dependencies, we compute the autocorrelation of the errors for N = 462storms (detected in 85 individual pixels) with durations larger than 4 hours. We then compare the resulting median and 90% confidence interval with those of N time series of random white noise with the same duration of the observed events. We find that, apart from MRMS that exhibits a certain degree of autocorrelation at lag 1, observed and synthetic autocorrelations are similar (Fig. S3). Based on these empirical outcomes, we consider the spatiotemporal dependencies among the random errors to be negligible for the purpose of applying the error model in our basin.

267

246

247

248

249

250

251

252

253

254

255

256

257

258

259

260

261

262

263

264

265

266

268

4.2. The Coupled Hydrologic-Hydraulic Model

4.2.1. Brief Model Description

269

270

271

272

273

274

275

276

277

278

279

280

281

282

283

284

285

286

287

288

289

290

291

SWMM is a semi-distributed rainfall-runoff model developed by the U.S. EPA (Koustas 2000) for simulating runoff in urban catchments. The model includes a hydrologic component that transforms rainfall into surface runoff in sub-catchments, and a routing component that transports this runoff through stormwater infrastructure elements, including pipes, channels, and storages. As detailed in the user's guide (W. James et al., 2010), different hydrologic processes can be simulated that allow applying the model in event-based or continuous fashion. The routing component includes several hydraulic modeling capabilities largely based on the application in one dimension (1D) of the momentum and continuity equations. The model domain is generated by (i) discretizing the catchment into smaller sub-catchments corresponding to each inlet into the infrastructure drainage system; and (ii) introducing different types of model elements, such as conduits, junctions (e.g., catch basins and manholes), outfall nodes, and storage units (see Table 1 for a description of the main elements). Model inputs include rainfall data, provided through one or more rain gages (or radar pixels; see Table 1), while outputs include, among others, the flow rate and hydraulic grade lines throughout the drainage system, and surface flood volumes when surcharge occurs (i.e., water rises above the crown of the highest conduit) and the hydraulic grade line exceeds surface elevation of the junctions. In addition to the standard components of SWMM, we also use the proprietary PCSWMM implementation to model overland routing of flood water and the resulting flood extent. This is accomplished through an integrated 1D-2D modeling approach where the fully dynamic 1D approach (i.e. SWMM) is extended to 2D free surface flow using a mesh that captures topography, geometry and built structures. PCSWMM builds upon the SWMM 1D

model and discretizes the domain into a square mesh where each 2D cell is represented with a 2D node or a junction, whose invert elevations are assigned as either the ground surface elevation or the rim elevation of adjacent coupled 1D junctions (Finney et al., 2012; R. James et al., 2013). In PCSWMM, rainfall-runoff processes and routing in the pipe system are simulated in 1D, as in SWMM. When flood conditions are simulated, water leaves the drainage system at catch basin junctions (and manholes, if not bolted) and is then routed on the 2D mesh cells. Flood water is routed across the land surface and, as the hydraulic grade line drops below the catch basin rim elevation, water can re-enter the drainage system.

4.2.2. Model Setup

To set up SWMM in our basin, we extensively pre-process and quality control the LiDAR and infrastructure data through Geographic Information System (GIS) software and field visits. We use the LiDAR point cloud data with average point spacing of 0.25 m and total point count of over 37.8 million in the basin to generate a Digital Elevation Model (DEM) at 0.6-m resolution for the catchment delineation. The elevations of the point cloud data range from 320 m to 484 m, mainly constituting returns from the road surface and roofs of the buildings. Features such as buildings are initially retained as they can influence sub-catchment boundaries. Next, we use the high-resolution DEM to generate 2D computational square grid cells at a lower resolution of 4.57 m (15 ft) for overland routing of flood waters needed for PCSWMM. This lower resolution is selected due to the high computational demands of routing overland flow. We then exclude buildings through a mask of building footprints available from ASU (2018), as they would artificially raise the grid cell elevation and impact overland flow routing. Using aerial imagery, we visually identify DEM and 2D cells with abnormally low or high elevations caused by the presence of overpasses or sites that were under construction when the LiDAR was

obtained. To prevent ponding at these artificial depressions, those sections are excluded from the 2D computational grid by creating bounding layers over them.

As a next step, we check the reliability of the GIS data of stormwater infrastructure components through field visits. During these, we verify surface structures (e.g., catch basins, manholes) in frequently flooded areas identified by project partners in the City of Phoenix and the FCDMC, as well as areas that deviated from standard design practice. In addition, we identify a few missing or moved surface components, including catch basins and manholes, as well as missing subsurface components where stormwater could not reach the outlet from a portion of the system as documented. These missing pipe segments are specified based on design standards. Additionally, some components have missing attribute data such as rim or invert elevations, slope, pipe diameter, and pipe material. Rim elevations are estimated from the DEM, while invert elevations, slope, pipe size, and material are estimated from adjacent components and design standards. Once data gaps are assessed and filled, the infrastructure shapefiles are imported into SWMM to create the drainage network in the model. Finally, pipe material (mostly concrete) is used to specify Manning's roughness coefficient (on average, 0.011).

We apply the model for event-based simulations using rainfall data from (i) the only gage of the FCDMC networks installed within the basin; and (ii) the radar grids (see Fig. 1b). For the hydrologic component, we specify the percent imperviousness of each sub-catchment using the NRCS dataset and we simulate infiltration with the Green-Ampt's method, which is parameterized with soil properties from the Web Soil Survey database. Parameter values are reported in Tables 2 and 3. The sub-catchments draining to each of the 26 drywells present in the basin are modeled as disconnected from the rest of the drainage system unless flooding and overland flow cross sub-catchment boundaries (modeled only in the 2D PCSWMM). We use the

1D dynamic wave routing method to model routing in the pipes. PCSWMM simulates surface flooding by coupling the 1D model of the drainage network with a 2D overland flow model. When surcharge occurs, flow exiting catch basins (all manholes are bolted in our study basin) is routed on the 4.57-m x 4.57-m mesh surface using the Saint-Venant flow equations.

4.3. Hydrologic-Hydraulic Simulations

338

339

340

341

342

343

344

345

346

347

348

349

350

351

352

353

354

355

356

357

358

359

360

We identify four storm events from the 2015-2019 study period with significant areal coverage in Phoenix, relatively high average precipitation depth, and for which NOAA has reported impacts on traffic and properties (NOAA, 2021). The storm characteristics are presented in Table 4. Two storms occurred in the middle of the NAM season and, as such, are of monsoonal origin; the other two were observed at the end of September and in October during the transition from NAM to winter weather conditions and, for one of them, the source of moisture came partially from a tropical storm (personal communication by Dr. Larry Hopper, at the NWS). Storm durations range from 6 to 30 hours and gage total rainfall varies from 5 to 10 mm. The impacts of one of the storms (September 23, 2019) on street level flooding in the study basin is presented in the photograph of Fig. 2 that was taken by a camera installed to monitor flooding during the event. For each storm, we conduct simulations with SWMM using different rainfall inputs at 1-h resolution, including (1) rain gage observations (R_g) ; (2) original (i.e., R_r^*) QPEs from Stage IV, MRMS and GCMRMS; and (3) an ensemble of N = 100 fields generated through the error model for each radar product. The rainfall inputs derived from the rain gage are spatially uniform, while those produced by the original radar products and the error model are spatially variable with a resolution of 4 km (1 km) for Stage IV (MRMS and GCMRMS), as also shown in Fig. 1b. The procedure used to generate N = 100 fields with the error model is based on Monte Carlo simulations, consisting of the following steps:

- 1. For a given storm with T time steps, the unconditional bias is first removed from the original radar estimates using equation (3) and the deterministic component $h(R_r)$ is calculated with equation (5) at all pixels and times.
- 364 2. Since the spatiotemporal dependencies of the errors are found to be negligible, for each pixel, a total of T random errors, $e(R_r)$, are randomly generated from the corresponding probability distribution.
- 367 3. The errors and the deterministic component $h(R_r)$ are then used to estimate the true rainfall using equation (2), resulting in T rainfall grids for each of the pixel. This spatiotemporal rainfall field represents a possible realization of the true rainfall for the analyzed event, given the original radar-derived QPEs. The spatiotemporal rainfall field is then used to force SWMM.
- 372 4. Steps 2 and 3 are repeated *N* times.

Since the 2D simulations with PCSWMM are computationally intensive, running this model N = 100 times is not feasible. Therefore, we select three rainfall sequences generated from the previous Monte Carlo SWMM simulations for each storm. These sequences correspond to the 25th, 50th, and 75th percentiles of the distribution of the total flood volume, V_f (i.e., volume of water that exits the drainage system through catch basins when the hydraulic grade line exceeds the rim elevation of catch basins) across the 100 Monte Carlo runs. We then apply PCSWMM for these three realizations for each storm to illustrate the influence of precipitation uncertainty on flood extent in a computationally efficient manner.

4.4. Uncertainty Quantification

Let $\{x_1, ..., x_N\}$ be the values of a given variable x (rainfall or discharge at a given time step) returned by the ensemble runs with the radar rainfall or the hydrologic model. We quantify

the uncertainty of these ensemble simulations of x through two simple metrics, including: (i) skewness of the distribution of $\{x_1, ..., x_N\}$; and (ii) interquartile range relative to the median: $RIQR = (q_{0.75} - q_{0.25})/q_{0.50} \times 100$, where q_p is the quantile of the empirical distribution of $\{x_1, ..., x_N\}$ associated with the non-exceedance probability p.

5. Results

5.1. Characterization of Radar QPE Uncertainty

The first step to apply the error model is to calculate the unconditional bias, B_0 , which is needed to compute R_r via equation (3). We find B_0 to be 1.26, 0.66, 0.76 for Stage IV, MRMS, and GCMRMS, respectively, indicating that original Stage IV (MRMS and GCMRMS) QPEs underestimate (overestimate) the gage observations. Fig. 3 presents the scatterplots between R_r and R_g (estimating the true rainfall, R_{true}) along with the lines obtained through the Epanechnikov kernel and the power law of equation (5) for cluster 2 (results for cluster 1 are reported in Fig. S4). All radar products exhibit a positive systematic bias that becomes larger as R_r increases, as found in previous work (e.g., Ciach et al., 2007; Villarini et al., 2014; Villarini & Krajewski, 2009, 2010b). The conditional bias for Stage IV QPEs is much smaller than that found for the MRMS and GCMRMS products. The errors for GCMRMS are slightly smaller (larger) than those of MRMS for $R_r \le 15$ mm/h ($R_r > 15$ mm/h), where most (less) data points lie.

As a next step, we use equation (2) to compute the errors, $e(R_r)$, quantifying the variability of radar rainfall estimates around the $h(R_r)$ lines. Fig. 4 shows the errors along with the empirical quantiles (dotted lines) derived with the Epanechnikov kernel for cluster 2 (results for cluster 1 are reported in Fig. S5). For all products, the distribution of the errors is positively skewed and, importantly, does not vary with R_r . Based on this empirical outcome, we adopt a parametric distribution with constant parameters (i.e., a distribution that does not change with

 R_r), as in Villarini et al. (2014). We find the mixture of three gamma distributions to be the most appropriate parametric distribution, as suggested by the lowest AIC values (Table S1). The quantiles derived from the mixed gamma distribution are shown in Fig. 4 with solid lines, while the comparison between empirical and parametric distributions is reported in Fig. 5 (Fig. S6 for cluster 1) and parameters of the gamma distribution for each radar product are summarized in Table 5. Fig. 5 reveals that, for all products, the distribution of the errors is very well reproduced up to about $e(R_r) = 5$; larger values of e are underestimated, but they only account for less than 0.5% of the sample.

5.2 Propagation of Uncertainty from Rainfall to Runoff

5.2.1. Rainfall Uncertainty

Fig. 6 presents, for each storm, the time series of rainfall recorded at the gage (R_g ; red dots) along with the basin mean areal rainfall estimated by the three radar QPEs (R_r^* ; blue dots) and simulated by the corresponding error model (boxplots displaying 50% and 90% confidence intervals of N = 100 values produced by the Monte Carlo runs). For all events, the radar products estimate nonzero rainfall in a larger number of time steps as compared to the gage. For the gage-corrected Stage IV, R_g is very close to both R_r^* and median of the Monte Carlo simulations. As previously discussed, MRMS QPEs are positively biased, so that R_r^* is in most cases larger than R_g and median of the error model simulations. This bias is reduced when the gage correction is applied in GCMRMS (see, e.g., event on July 10, 2018). For all three products, higher rainfall measurements yield a higher magnitude of uncertainty for the error model. Finally, Table 6 presents the mean skewness and RIQR of the ensemble hourly rainfall across each storm duration. Due to the positive skewness of the distribution of the residual error in the radar error model (see Fig. 4), the mean skewness of the simulated rainfall is also positive and included

between 1.0 and 3.2, with higher values for Stage IV, followed by MRMS and GCMRMS. The relative variability across the ensemble members is quantified via the *RIQR*, whose average ranges from 56.1% to 74.6%, with the highest (lowest) values found again for Stage IV (GCMRMS).

5.2.2. Uncertainty of Basin-Integrated Runoff

430

431

432

433

434

435

436

437

438

439

440

441

442

443

444

445

446

447

448

449

450

451

452

We start evaluating the propagation of rainfall uncertainty into runoff by first assessing the variations in the outlet hydrograph (i.e., outflow at the pipe that discharges to the Salt River) across radar products and storms. The hydrographs simulated by the SWMM model under the rainfall forcings of Fig. 6 are displayed in Fig. 7. The use of Stage IV QPEs and rain gage observations as inputs for SWMM leads to closely aligned hydrographs, which are also very similar to the median hydrograph of the corresponding ensemble simulations. In contrast, the outflow generated by the original MRMS QPEs is consistently biased high compared to the simulation under the gage rainfall observations, with the median of ensemble runs falling between the two. As found in Fig. 6 for the rainfall values, the gage correction of MRMS QPEs reduces the bias in the resulting flow, as shown in the hydrographs with GCMRMS forcings. The uncertainty of the ensemble hydrologic simulations is quantified in Table 6 via the time-averaged skewness and RIOR of the discharge at the outlet. The mean skewness is still positive with values in the range 0.4–2.5, which are lower compared to those found for rainfall. This is also true for the mean RIQR that varies from 22.4% to 66.9%. Metric values are, again, the largest (smallest) for Stage IV (GCMRMS).

To complement the information provided by the hydrographs at the catchment outlet and better assess flood impacts and differences across precipitation inputs, we examine additional metrics simulated by SWMM. These include Q_{max} : peak flow of the hydrograph at the outlet; and

V_f: stormwater volume that ponds on the surface of the catchment when the hydraulic grade line reaches the catch basin rim elevation at one or more locations. In addition, we consider two metrics that characterize the hydraulic response of the stormwater pipe system under surcharge conditions, including t_{max} : maximum total duration of node surcharging across all nodes; and h_{max} : maximum height of the hydraulic grade line above pipe invert level. Note that nonzero values for t_{max} and h_{max} do not necessarily imply surface flooding, as mentioned in section 4.2.1. Fig. 8 presents the simulated metric values for each storm and radar product. Simulations under gage rainfall, R_g , could be used as reference to compare across storms. The lowest (highest) Q_{max} and V_f are obtained for the storm on September 23, 2019 (October 7, 2018), which are characterized by the lowest (highest) rainfall intensity (see Table 4). h_{max} exhibits a certain relation with Q_{max} and V_f that quantify actual surface flooding, while t_{max} is largely controlled by storm duration (reported in Table 4). Turning now our attention to the radar products, all metrics modeled with R_g are close to those simulated under Stage IV R_r^* and in most cases (all cases except t_{max} for event 1) within the 50% (90%) confidence interval of the ensemble runs. When compared to the metrics simulated under R_g , simulations with MRMS rainfall products lead to longer t_{max} in two events and larger h_{max} , Q_{max} , V_f in most storms. The use of GCMRMS improves MRMS performance, apart from some metrics in individual storms (e.g., h_{max} on September 23, 2019; V_f on July 24, 2017). Finally, when considering the spread of the ensemble distributions, there is not a specific radar product that leads to wider or narrower distributions for a given metric across all events. These metrics are further discussed in Section 6.

5.2.3. Uncertainty of Spatial Flooding

453

454

455

456

457

458

459

460

461

462

463

464

465

466

467

468

469

470

471

472

473

474

475

The metrics presented in Fig. 8 aid in comparing model output across simulations.

However, information on location and extent of flooding over time is needed to alert residents to

dangerous conditions, provide timely emergency response, and identify critical locations for infrastructure investment. Such information is obtained through the 2D simulations of flood routing with PCSWMM. Figs. 9 and 10 illustrate the uncertainty in maximum flood extent (i.e., areas that are flooded for at least one time step) simulated under each radar product for the storms on July 31, 2018 and October 7, 2018, respectively (Figs. S7 and S8 show results for the other two storms). Uncertainty is captured through the simulations under the rainfall fields of the error model associated with the 25^{th} percentile (blue), median (green), and 75^{th} percentile (red) of the distribution of V_f from the 1D SWMM simulations. Thus, if a pixel is blue, flooding has been simulated for all higher percentiles; when it is green, it has been simulated for the median and 75^{th} percentile; and when the pixel color is red, flooding only occurred for the 75^{th} percentile.

For the monsoonal storm on July 31, 2018, the use of rainfall fields generated by the error model with Stage IV QPEs (Figs. 9a-c) leads to simulation of street flooding in two distinct basin locations (Figs. 9b,c), with a total of 0.001, 0.03, and 0.05 km² of flooded areas for the 25th percentile, median and 75th percentile, respectively. If rainfall forcings are provided by MRMS (Figs. 9d-f), street flooding is also predicted in a location in the upper part of the basin (Figs. 9d,f). Given the positive bias of these QPEs, the simulated flooding extent is larger and equal to 0.07 (0.23) km² for the 25th (75th) percentile. Interestingly, the uncertainty across the percentiles is low in a relatively large region in the lower part of the catchment (blue area in Fig. 9e). The gage correction of MRMS QPEs performed for GCMRMS leads to results that are substantially similar to Stage IV (Figs. 9g-i). Maps of flooded areas for the transition storm on October 7, 2018 are reported in Fig. 10. Flooding is predicted in two of the same basin regions displayed in Fig. 9. Flooded areas under Stage IV (Figs. 10a,b) are very similar for the median (0.16 km²) and 75th percentile (0.19 km²), while they decrease substantially for the 25th percentile (0.006 km²).

As found for the monsoonal storm of Fig. 9, using MRMS QPEs (Figs. 10c,d) as model inputs increases the extent of street level flooding as compared to Stage IV, which reaches 0.04 (0.4 km²) for the 25th (75th) percentiles. The adoption of GCMRMS (Figs. 10e,f) leads instead to lower flooded areas compared to Stage IV, ranging from no flooded areas for the 25th percentiles to 0.09 km² for the 75th percentile.

6. Discussion

While focused on an urban catchment in the Phoenix metropolitan area, results of our modeling effort are based on extensive precipitation, land surface, and infrastructure datasets, and, as such, they provide general insights on the utility of radar QPEs and hydrologic-hydraulic models for urban flood predictions in the NAM region and other areas, as discussed in the next subsections.

6.1. Comparison of Radar Products and their Utility for Urban Flood Modeling

When applying the error model using the network of 168 gages, we find that, on average, Stage IV QPEs underestimate gage rainfall by ~20%, while MRMRS and GCMRMS overestimate it by about 51% and 31%, respectively (see values of B_0 reported in section 5.1). Qualitatively, this result is also confirmed for the four simulated storm events. Our finding is consistent with the extensive comparison of six radar products, including Stage IV and earlier versions of MRMS and GCMRMS, performed by Seo et al. (2018) in Iowa, but opposite to two separate analyses by Lin et al. (2018) and Gao et al. (2021) in Texas during a set of flood events. The existence of regional differences in performance of Stage IV and MRMRS have been also recently highlighted in another comparison study in Louisiana by Sharif et al. (2020). Overall, results of our and other studies suggest that radar-only QPEs are critically improved through gage-based bias corrections, as done in Stage IV and GCMRMS.

Fig. 6 shows that nonzero rainfall is observed by the radar QPEs in more time steps compared to the single point measurement of the gage, indicating that, even in a very small basin, a single gage may be unable to monitor localized monsoonal convective storms. Despite this, Figs. 6 and 7 show that flood simulations under the more accurate Stage IV-derived rainfall products lead to very similar outcomes to those obtained with gage rainfall, R_g . This suggests two considerations. First, while the basin area is small, the presence of stormwater infrastructure acts as an integrator of the rainfall spatiotemporal variability, so that, despite differences between R_g and Stage IV QPEs, the resulting flood simulations are substantially quite similar. Second, an important consequence of the first consideration is that, when gage observations are not available, hydrologic simulations with Stage IV QPEs (available throughout the country) can provide a reliable reference for evaluating the impacts of urban flooding. On the other hand, in our study basin, the use of MRMS QPEs consistently results in the largest flood volumes and extent, while the flooding impacts simulated with GCMRMS QPEs are similar to those obtained with Stage IV (see Figs. 8-10). Thus, our effort demonstrates that the gage correction applied to MRMS greatly improves the utility of this radar-only product for flood modeling.

522

523

524

525

526

527

528

529

530

531

532

533

534

535

536

537

538

539

540

541

542

543

544

6.2. Uncertainty of Radar Rainfall and Corresponding Urban Flood Simulations

Radar QPEs can provide key support for urban flood forecasting and management, complementing gage observations that may only be available at sparse location and not in real time. However, radar products are affected by different sources of errors, thus requiring models to characterize the associated uncertainty. Here, we use an error model with a multiplicative structure that leads to largest uncertainties for the highest rainfall values (see Fig. 6), as also found in previous applications (Villarini et al. 2014). As a consequence, the uncertainty of urban flood predictions is expected to be also relatively high, as these higher precipitation observations

are more likely to result in flooding. This is in general confirmed by our results because the largest spread of the basin outflow confidence intervals occurs right after the highest rainfall events (see Figs. 6 and Fig. 7). However, a closer look at the uncertainty metrics for rainfall and discharge reported in Table 6 suggests that the hydrologic processes governing the rainfall-runoff transformation have two effects: (i) they smooth the impact of the highest rainfall values simulated by the error model, so that the distribution of the ensemble outflows is more symmetric (i.e., less positively skewed) than the distribution of the rainfall inputs, as also found by Grimley et al. (2020); and (ii) they reduce the relative spread of the ensemble rainfall distribution, as shown by the mean *RIQR* decreasing from an average of 64.7% to 48.2% when considering all events and radar products. These conclusions should be refined in future work quantifying the effect of other sources of uncertainty for the hydrologic-hydraulic model.

We also highlight that the uncertainty of the basin outflow is greater in the rising than the falling limb of the hydrographs (Fig. 7). Specifically, across all storms and radar products, the 50% (90%) confidence interval range in the falling limb is, on average, just 8.8% (6.3%) of the range in the rising limb. This behavior can be explained considering that, in highly impervious areas and small watersheds, the rising limb and its associated uncertainty are strongly shaped by the rainfall rate. In contrast, during the falling limb of the hydrograph, catchment and drainage network properties exert a larger control that results in an uncertainty reduction. When considering the other flood metrics characterizing surface flooding and surcharge conditions in the stormwater infrastructure, we find that their uncertainty varies substantially (Fig. 8). As expected, the variability of Q_{max} is related to the QPE uncertainty, although the ensemble distributions for Q_{max} are more symmetric for the same reasons mentioned above. The distribution of V_T is highly skewed with several zero values, despite t_{max} and t_{max} are never zero.

This implies that a fraction of QPEs with lower values leads to surcharge conditions but not to surface flooding. The uncertainty of t_{max} is practically negligible, indicating that all precipitation inputs lead to surcharge conditions over very similar maximum durations. In contrast, h_{max} , which quantifies the severity of surcharge conditions, exhibits a variability (mainly in the range of 5 m) due to the different QPE values simulated by the error model.

6.3. Utility for Urban Flood Management

568

569

570

571

572

573

574

575

576

577

578

579

580

581

582

583

584

585

586

587

588

589

590

Urban pluvial flooding is characterized by localized damage to property and impacts to pedestrian and vehicle travel. Timely information on the location and severity of these hazards can enable response and limit travel delays and risks (NWS, 2021). Our simulations with PCSWMM show that, despite uncertainties and biases across radar products, all of them robustly identify the same basin regions experiencing flooding conditions (Figs. 9, 10, S7 and S8). This is a promising result supporting the operational use of QPFs derived from radar QPEs combined with hydrologic-hydraulic models, as also highlighted by Grimley et al. (2020) when discussing their simulation of pluvial flooding in an urban area in Iowa. However, the extent of flooding areas exhibits differences both for the same radar product and across radar products. The latter ones can be significant when the QPE bias is high, as found for MRMS. Therefore, flood response can confidently target the correct areas within a few blocks, though the precise flood extent remains uncertain. Improvements in QPEs accuracy are then expected to greatly benefit prioritization and response measures during floods. These findings are driven by both catchment topography and the design of the drainage network; therefore, the flood management implications of the residual uncertainty may vary by location.

It must also be noted that the SWMM model has its own structural and parametric uncertainties (Abily et al., 2016; Deletic et al., 2012). While fully assessing these is out the scope

of the current analysis, it is important to consider that the uncertainty in flood estimates simulated in our study for an ensemble of QPEs incorporate other uncertainty sources in the SWMM model. The flood metrics and maps (Figs. 8-10) also point to the need for flood extent and depth data in urban areas to properly validate the accuracy of these hydrologic and hydraulic simulations. New hydrological sensing approaches such as citizen science (Assumpção et al., 2018; Fava et al., 2019) and image-based sensing (Hostache et al., 2018; Tauro et al., 2017) offer opportunities to sense flooding as it occurs at the urban scale. These emerging approaches could enable error assessment of the urban hydrological model, providing further context to interpret the propagation of precipitation uncertainty into urban flooding.

7 Conclusions

The small size and heterogeneity of urban catchments, combined with the short, highintensity precipitation events that drive pluvial flooding, make accurate and efficient urban
pluvial flood modeling an ongoing research challenge (Bermúdez et al., 2018; Blanc et al., 2012;
van Dijk et al., 2014). This is especially true in the NAM region, which is dominated by highintensity convective thunderstorms. In this work, we provide insights on pluvial flooding by
assessing the propagation of radar precipitation uncertainty into flood modeling in a 2.38-km²
urban catchment in Phoenix, AZ. Our results, based on simulations for four events during the
NAM, can be summarized as follows:

(1) While Stage IV QPEs slightly underestimate gage rainfall (on average, by 20%), the resulting
flood predictions are similar to those obtained with rain gage records, suggesting that Stage
IV QPEs are reliable products for modeling urban flooding. MRMS QPEs are positively
biased (+51%) and so are the flood peaks and extent of flooded areas simulated with these

products. The gage correction performed in GCMRMS leads to results similar to Stage IV.

- (2) The QPE uncertainty simulated by the error model increases with rainfall rate and is rather alike across the three radar products. This is also true for the resulting flood metrics.
- (3) As a result of the rainfall-runoff transformation processes and the presence of stormwater infrastructure, uncertainty of flood metrics is reduced and less positively skewed when compared with the QPE uncertainty. The uncertainty may vary significantly depending on the metrics that capture different flooding features (e.g., pipe flow, surface flooding, and pipe surcharge conditions).
- (4) All radar products lead to the identification of the same flooded areas within an extent of a few blocks in the basin. This is a promising result for the use of radar-derived QPEs and hydrologic-hydraulic models for urban pluvial flood modeling. However, the exact location and extent of flooded areas may vary significantly across products, suggesting that increasing QPE accuracy can greatly benefit flood management and forecasting agencies.

627 Acknowledgments

We thank two anonymous reviewers whose comments helped improve the quality of the manuscript. We also thank Dr. Larry Hopper and Mr. Paul Iñiguez from the NWS Phoenix Office for their insights on quality of radar QPEs and selection of storm events in the Phoenix metropolitan regions. This work has been supported by the National Science Foundation (NSF) Award "SCC: Community-Based Automated Information for Urban Flooding" (Award 1831475), and by the UCAR COMET Award "Assessing the Accuracy of Multi-Radar/Multi-Sensor (MRMS) Precipitation Estimates in the Phoenix Metropolitan Area to Support Flash Flood Warning Operations" (Award SUBAWD001574).

References

637

638 Abily, M., Bertrand, N., Delestre, O., Gourbesville, P., & Duluc, C.-M. (2016). Spatial Global 639 Sensitivity Analysis of High Resolution classified topographic data use in 2D urban flood 640 modelling. Environmental Modelling & Software, 77, 183–195. https://doi.org/10.1016/j.envsoft.2015.12.002 641 642 Adams, D. K., & Comrie, A. C. (1997). The North American Monsoon. Bulletin of the American 643 *Meteorological Society*, 78(10), 18. 644 Akaike, H. (1974). A new look at the statistical model identification. *IEEE Transactions on* 645 Automatic Control, 19(6), 716–723. https://doi.org/10.1109/TAC.1974.1100705 646 Assumpção, T. H., Popescu, I., Jonoski, A., & Solomatine, D. P. (2018). Citizen observations 647 contributing to flood modelling: Opportunities and challenges. Hydrology and Earth System Sciences, 22(2), 1473–1489. 648 649 ASU. (2018). Metro Phoenix USGS LiDAR Data. 650 https://asu.maps.arcgis.com/apps/webappviewer/index.html?id=0372792855514dd3bf96 651 54c20bbe10e6 652 Balling, R., & Brazel, S. (1987). Diurnal Variations in Arizona Monsoon Precipitation 653 Frequencies. *Monthly Weather Review*. 654 Bermúdez, M., Ntegeka, V., Wolfs, V., & Willems, P. (2018). Development and comparison of 655 two fast surrogate models for urban pluvial flood simulations. Water Resources 656 Management, 32(8), 2801–2815. 657 Blanc, J., Hall, J. W., Roche, N., Dawson, R. J., Cesses, Y., Burton, A., & Kilsby, C. G. (2012). 658 Enhanced efficiency of pluvial flood risk estimation in urban areas using spatial659 temporal rainfall simulations. Journal of Flood Risk Management, 5(2), 143–152. 660 https://doi.org/10.1111/j.1753-318X.2012.01135.x 661 Chen, J., Hill, A. A., & Urbano, L. D. (2009). A GIS-based model for urban flood inundation. 662 Journal of Hydrology, 373(1-2), 184-192. https://doi.org/10.1016/j.jhydrol.2009.04.021 663 Ciach, G. J., & Gebremichael, M. (2020). Empirical distribution of conditional errors in radar 664 rainfall products. Geophysical Research Letters, 47(22), e2020GL090237. https://doi.org/10.1029/2020GL090237 665 666 Ciach, G. J., & Krajewski, W. F. (2006). Analysis and modeling of spatial correlation structure 667 in small-scale rainfall in Central Oklahoma. Advances in Water Resources, 29(10), 1450– 668 1463. 669 Ciach, G. J., Krajewski, W. F., & Villarini, G. (2007). Product-Error-Driven Uncertainty Model 670 for Probabilistic Quantitative Precipitation Estimation with NEXRAD Data. Journal of 671 Hydrometeorology, 8(6), 1325–1347. https://doi.org/10.1175/2007JHM814.1 672 Cohen, B. (2006). Urbanization in developing countries: Current trends, future projections, and 673 key challenges for sustainability. *Technology in Society*, 28(1–2), 63–80. 674 https://doi.org/10.1016/j.techsoc.2005.10.005 675 Cristiano, E., ten Veldhuis, M.-C., & van de Giesen, N. (2017). Spatial and temporal variability 676 of rainfall and their effects on hydrological response in urban areas – a review. 677 Hydrology and Earth System Sciences, 21(7), 3859–3878. https://doi.org/10.5194/hess-678 21-3859-2017 679 Dai, Q., Yang, Q., Zhang, J., & Zhang, S. (2018). Impact of gauge representative error on a radar 680 rainfall uncertainty model. Journal of Applied Meteorology and Climatology, 57(12), 681 2769–2787.

682	Deletic, A., Dotto, C. B. S., McCarthy, D. T., Kleidorfer, M., Freni, G., Mannina, G., Uhl, M.,
683	Henrichs, M., Fletcher, T. D., Rauch, W., Bertrand-Krajewski, J. L., & Tait, S. (2012).
684	Assessing uncertainties in urban drainage models. Physics and Chemistry of the Earth,
685	Parts A/B/C, 42–44, 3–10. https://doi.org/10.1016/j.pce.2011.04.007
686	Doocy, S., Daniels, A., Murray, S., & Kirsch, T. D. (2013). The Human Impact of Floods: A
687	Historical Review of Events 1980-2009 and Systematic Literature Review. PLoS
688	Currents. https://doi.org/10.1371/currents.dis.f4deb457904936b07c09daa98ee8171a
689	Emanuel, K. (2005). Increasing destructiveness of tropical cyclones over the past 30 years.
690	Nature, 436(7051), 686-688. https://doi.org/10.1038/nature03906
691	Fang, HB., Fang, KT., & Kotz, S. (2002). The meta-elliptical distributions with given
692	marginals. Journal of Multivariate Analysis, 82(1), 1–16.
693	Fava, M. C., Abe, N., Restrepo-Estrada, C., Kimura, B. Y. L., & Mendiondo, E. M. (2019).
694	Flood modelling using synthesised citizen science urban streamflow observations.
695	Journal of Flood Risk Management, 12(S2), e12498. https://doi.org/10.1111/jfr3.12498
696	Finney, K., James, R., & Perera, N. (2012). Benchmarking SWMM5/PCSWMM 2D Model
697	Performance. International Conference on Water Management Modeling.
698	Gao, S., Zhang, J., Li, D., Jiang, H., & Fang, Z. N. (2021). Evaluation of Multiradar Multisenson
699	and Stage IV Quantitative Precipitation Estimates during Hurricane Harvey. Natural
700	Hazards Review, 22(1), 04020057. https://doi.org/10.1061/(ASCE)NH.1527-
701	6996.0000435
702	Germann, U., Berenguer, M., Sempere-Torres, D., & Zappa, M. (2009). REAL-Ensemble radar
703	precipitation estimation for hydrology in a mountainous region. Quarterly Journal of the
704	Royal Meteorological Society, 135(639), 445–456. https://doi.org/10.1002/qj.375

705 Grimley, L. E., Quintero, F., & Krajewski, W. F. (2020). Streamflow Predictions in a Small 706 Urban-Rural Watershed: The Effects of Radar Rainfall Resolution and Urban Rainfall-707 Runoff Dynamics. *Atmosphere*, 11(8), 774. https://doi.org/10.1175/1525-708 7541(2001)002<0621:EORIC>2.0.CO;2 709 Guan, X., Mascaro, G., Sampson, D., & Maciejewski, R. (2020). A metropolitan scale water 710 management analysis of the food-energy-water nexus. Science of The Total Environment, 711 701, 134478. https://doi.org/10.1016/j.scitotenv.2019.134478 712 Habib, E., Aduvala, A. V., & Meselhe, E. A. (2008). Analysis of radar-rainfall error 713 characteristics and implications for streamflow simulation uncertainty. Hydrological 714 Sciences Journal, 53(3), 568–587. https://doi.org/10.1623/hysj.53.3.568 715 Hossain, F., Arnold, J., Beighley, E., Brown, C., Burian, S., Chen, J., Madadgar, S., Mitra, A., 716 Niyogi, D., Pielke, R., Tidwell, V., & Wegner, D. (2015). Local-To-Regional Landscape 717 Drivers of Extreme Weather and Climate: Implications for Water Infrastructure 718 Resilience. *Journal of Hydrologic Engineering*, 20(7), 02515002. 719 https://doi.org/10.1061/(ASCE)HE.1943-5584.0001210 720 Hostache, R., Chini, M., Giustarini, L., Neal, J., Kavetski, D., Wood, M., Corato, G., Pelich, R.-721 M., & Matgen, P. (2018). Near-Real-Time Assimilation of SAR-Derived Flood Maps for 722 Improving Flood Forecasts. Water Resources Research, 54(8), 5516–5535. 723 https://doi.org/10.1029/2017WR022205 724 James, R., Finney, K., Perera, N., James, B., & Peyron, N. (2013). SWMM5/PCSWMM 725 Integrated 1D-2D Modeling. In U. E. (retired); M. B. Jr. A.S. Donigian, AQUA TERRA 726 Consultants; Richard Field (Ed.), Fifty Years Of Watershed Modeling—Past, Present And 727 Future. ECI Symposium Series. http://dc.engconfintl.org/watershed/12.

- James, W., Rossman, L. E., & James, W. R. C. (2010). User's Guide to SWMM5, 13th Edition.
- Kirstetter, P.-E., Delrieu, G., Boudevillain, B., & Obled, C. (2010). Toward an error model for
- radar quantitative precipitation estimation in the Cévennes–Vivarais region, France.
- 731 *Journal of Hydrology*, 394(1–2), 28–41. https://doi.org/10.1016/j.jhydrol.2010.01.009
- Koustas, R. (2000). Update on EPA'S Urban Watershed Management Branch Modeling
- 733 Activities. *Journal of Water Management Modeling*.
- 734 https://doi.org/10.14796/JWMM.R206-21
- Leandro, J., Schumann, A., & Pfister, A. (2016). A step towards considering the spatial
- heterogeneity of urban key features in urban hydrology flood modelling. *Journal of*
- 737 *Hydrology*, 535, 356–365. https://doi.org/10.1016/j.jhydrol.2016.01.060
- Li, J., Gao, X., Maddox, R. A., Sorooshian, S., & Hsu, K. (2003). Summer Weather Simulation
- for the Semiarid Lower Colorado River Basin: Case Tests. *MONTHLY WEATHER*
- 740 *REVIEW*, 131, 21.
- Lin, P., Hopper, L. J., Yang, Z.-L., Lenz, M., & Zeitler, J. W. (2018). Insights into
- Hydrometeorological Factors Constraining Flood Prediction Skill during the May and
- October 2015 Texas Hill Country Flood Events. *Journal of Hydrometeorology*, 19(8),
- 744 1339–1361. https://doi.org/10.1175/JHM-D-18-0038.1
- 745 Lin, Y. (2020). GCIP/EOP Surface: Precipitation NCEP/EMC 4KM Gridded Data (GRIB) Stage
- 746 IV Data. Version 1.0 (1.0, p. 229482 data files, 2 ancillary/documentation files, 11 GiB)
- 747 [GNU Zip Compressed (.gz) Gridded Binary (GRIB) Format (application/x-gzip), GNU
- 748 Zip (.gz) Format (application/x-gzip)]. UCAR/NCAR Earth Observing Laboratory.
- 749 https://doi.org/10.5065/D6PG1QDD

750	Mascaro, G., Deidda, R., & Hellies, M. (2013). On the nature of rainfall intermittency as
751	revealed by different metrics and sampling approaches. Hydrology and Earth System
752	Sciences, 17(1), 355-369. https://doi.org/10.5194/hess-17-355-2013
753	Mascaro, Giuseppe. (2017). Multiscale Spatial and Temporal Statistical Properties of Rainfall in
754	Central Arizona. Journal of Hydrometeorology, 18(1), 227–245.
755	https://doi.org/10.1175/JHM-D-16-0167.1
756	Mascaro, Giuseppe. (2018). On the distributions of annual and seasonal daily rainfall extremes in
757	central Arizona and their spatial variability. Journal of Hydrology, 559, 266-281.
758	https://doi.org/10.1016/j.jhydrol.2018.02.011
759	Mascaro, Giuseppe. (2020). Comparison of Local, Regional, and Scaling Models for Rainfall
760	Intensity-Duration-Frequency Analysis. Journal of Applied Meteorology and
761	Climatology.
762	MRLC. (2016). Multi-Resolution Land Characteristics (MRLC) Consortium Multi-Resolution
763	Land Characteristics (MRLC) Consortium. https://www.mrlc.gov/
764	Nelson, B. R., Prat, O. P., Seo, DJ., & Habib, E. (2016). Assessment and Implications of NCEP
765	Stage IV Quantitative Precipitation Estimates for Product Intercomparisons. Weather and
766	Forecasting, 31(2), 371–394. https://doi.org/10.1175/WAF-D-14-00112.1
767	NOAA. (2016). National Water Model: Improving NOAA's Water Prediction Services
768	[Water.noaa.gov]. Office of Water Prediction. https://water.noaa.gov/documents/wrn-
769	national-water-model.pdf
770	NOAA. (2020). Flood Related Products. NOAA's National Weather Service.
771	https://www.weather.gov/safety/flood-products

772 NOAA. (2021). Storm Data Publication: IPS: National Climatic Data Center (NCDC). National 773 Centers for Environmental Information. https://www.ncdc.noaa.gov/IPS/sd/sd.html 774 NRCS. (2019). Web Soil Survey—Home. 775 https://websoilsurvey.sc.egov.usda.gov/App/HomePage.htm 776 NWS. (2021). Flood Safety Rules. NOAA's National Weather Service. 777 https://www.weather.gov/mlb/flashflood rules 778 Prein, A. F., Liu, C., Ikeda, K., Trier, S. B., Rasmussen, R. M., Holland, G. J., & Clark, M. P. 779 (2017). Increased rainfall volume from future convective storms in the US. Nature 780 Climate Change, 7(12), 880–884. https://doi.org/10.1038/s41558-017-0007-7 781 Rogers, J. W., Cohen, A. E., & Carlaw, L. B. (2017). Convection during the North American 782 Monsoon across Central and Southern Arizona: Applications to Operational 783 Meteorology. Weather and Forecasting, 32(2), 377–390. https://doi.org/10.1175/WAF-784 D-15-0097.1 785 Rosenzweig, B. R., McPhillips, L., Chang, H., Cheng, C., Welty, C., Matsler, M., Iwaniec, D., & 786 Davidson, C. I. (2018). Pluvial flood risk and opportunities for resilience. WIREs Water, 787 5(6). https://doi.org/10.1002/wat2.1302 788 Rossman, L. A. (2010). Stormwater management model user's manual, version 5.0. National 789 Risk Management Research Laboratory, Office of Research and Development, US 790 Environmental Protection Agency. 791 https://cfpub.epa.gov/si/si public record report.cfm?Lab=NRMRL&dirEntryId=114231 792 Saber, M., Abdrabo, K. I., Habiba, O. M., Kantosh, S. A., & Sumi, T. (2020). Impacts of Triple 793 Factors on Flash Flood Vulnerability in Egypt: Urban Growth, Extreme Climate, and

Mismanagement. Geosciences, 10(1), 24. https://doi.org/10.3390/geosciences10010024

794

795	Salas, F. R., Somos-Valenzuela, M. A., Dugger, A., Maidment, D. R., Gochis, D. J., David, C.
796	H., Yu, W., Ding, D., Clark, E. P., & Noman, N. (2018). Towards Real-Time Continental
797	Scale Streamflow Simulation in Continuous and Discrete Space. JAWRA Journal of the
798	American Water Resources Association, 54(1), 7-27. https://doi.org/10.1111/1752-
799	1688.12586
800	Seo, BC., Krajewski, W. F., Quintero, F., ElSaadani, M., Goska, R., Cunha, L. K., Dolan, B.,
801	Wolff, D. B., Smith, J. A., Rutledge, S. A., & Petersen, W. A. (2018). Comprehensive
802	Evaluation of the IFloodS Radar Rainfall Products for Hydrologic Applications. Journal
803	of Hydrometeorology, 19(11), 1793–1813. https://doi.org/10.1175/JHM-D-18-0080.1
804	Seo, D., Lakhankar, T., Mejia, J., Cosgrove, B., & Khanbilvardi, R. (2013). Evaluation of
805	Operational National Weather Service Gridded Flash Flood Guidance over the Arkansas
806	Red River Basin. JAWRA Journal of the American Water Resources Association, 49(6),
807	1296–1307. https://doi.org/10.1111/jawr.12087
808	Serinaldi, F. (2008). Analysis of inter-gauge dependence by Kendall's τK, upper tail dependence
809	coefficient, and 2-copulas with application to rainfall fields. Stochastic Environmental
810	Research and Risk Assessment, 22(6), 671-688. https://doi.org/10.1007/s00477-007-
811	0176-4
812	Sharif, R. B., Habib, E. H., & ElSaadani, M. (2020). Evaluation of Radar-Rainfall Products over
813	Coastal Louisiana. <i>Remote Sensing</i> , 12(9), 1477. https://doi.org/10.3390/rs12091477
814	Sheppard, P., Comrie, A., Packin, G., Angersbach, K., & Hughes, M. (2002). The climate of the
815	US Southwest. Climate Research, 21, 219–238. https://doi.org/10.3354/cr021219

816	Tang, L., Tian, Y., Yan, F., & Habib, E. (2015). An improved procedure for the validation of
817	satellite-based precipitation estimates. Atmospheric Research, 163, 61-73.
818	https://doi.org/10.1016/j.atmosres.2014.12.016
819	Tauro, F., Piscopia, R., & Grimaldi, S. (2017). Streamflow Observations From Cameras: Large-
820	Scale Particle Image Velocimetry or Particle Tracking Velocimetry? Water Resources
821	Research, 53(12), 10374–10394. https://doi.org/10.1002/2017WR020848
822	ten Veldhuis, J. A. E. (2011). How the choice of flood damage metrics influences urban flood
823	risk assessment: Urban flood risk assessment. Journal of Flood Risk Management, 4(4),
824	281–287. https://doi.org/10.1111/j.1753-318X.2011.01112.x
825	Thakali, R., Kalra, A., & Ahmad, S. (2016). Understanding the Effects of Climate Change on
826	Urban Stormwater Infrastructures in the Las Vegas Valley. Hydrology, 3(4), 34.
827	https://doi.org/10.3390/hydrology3040034
828	The National Academies Press. (2019). Framing the Challenge of Urban Flooding in the United
829	States. The National Academies Press. https://doi.org/10.17226/25381
830	Tian, Y., Huffman, G. J., Adler, R. F., Tang, L., Sapiano, M., Maggioni, V., & Wu, H. (2013).
831	Modeling errors in daily precipitation measurements: Additive or multiplicative?:
832	MODELING ERRORS IN PRECIPITATION DATA. Geophysical Research Letters,
833	40(10), 2060–2065. https://doi.org/10.1002/grl.50320
834	Trenberth, K. E., Dai, A., Rasmussen, R. M., & Parsons, D. B. (2003). The Changing Character
835	of Precipitation. Bulletin of the American Meteorological Society, 84(9), 1205–1218.
836	https://doi.org/10.1175/BAMS-84-9-1205

837	van Dijk, E., van der Meulen, J., Kluck, J., & Straatman, J. H. M. (2014). Comparing modelling
838	techniques for analysing urban pluvial flooding. Water Science and Technology, 69(2),
839	305–311.
840	Villarini, G., & Krajewski, W. F. (2009). Empirically based modelling of radar-rainfall
841	uncertainties for a C-band radar at different time-scales: RADAR-RAINFALL
842	UNCERTAINTIES FOR A C-BAND RADAR. Quarterly Journal of the Royal
843	Meteorological Society, 135(643), 1424–1438. https://doi.org/10.1002/qj.454
844	Villarini, G., & Krajewski, W. F. (2010a). Review of the Different Sources of Uncertainty in
845	Single Polarization Radar-Based Estimates of Rainfall. Surveys in Geophysics, 31(1),
846	107–129. https://doi.org/10.1007/s10712-009-9079-x
847	Villarini, G., & Krajewski, W. F. (2010b). Sensitivity Studies of the Models of Radar-Rainfall
848	Uncertainties. Journal of Applied Meteorology and Climatology, 49(2), 288-309.
849	https://doi.org/10.1175/2009JAMC2188.1
850	Villarini, G., Seo, BC., Serinaldi, F., & Krajewski, W. F. (2014). Spatial and temporal
851	modeling of radar rainfall uncertainties. Atmospheric Research, 135–136, 91–101.
852	https://doi.org/10.1016/j.atmosres.2013.09.007
853	Yang, L., Smith, J., Baeck, M. L., & Morin, E. (2019). Flash flooding in arid/semiarid regions:
854	Climatological analyses of flood-producing storms in central arizona during the North
855	American monsoon. Journal of Hydrometeorology, 20(7), 1449–1471.
856	https://doi.org/10.1175/JHM-D-19-0016.1
857	Yang, L., Smith, J., Baeck, M. L., Morin, E., & Goodrich, D. C. (2017). Flash Flooding in
858	Arid/Semiarid Regions: Dissecting the Hydrometeorology and Hydrology of the 19

859	August 2014 Storm and Flood Hydroclimatology in Arizona. Journal of
860	Hydrometeorology, 18(12), 3103–3123. https://doi.org/10.1175/JHM-D-17-0089.1
861	Zhang, J., Howard, K., Langston, C., Kaney, B., Qi, Y., Tang, L., Grams, H., Wang, Y., Cocks,
862	S., Martinaitis, S., Arthur, A., Cooper, K., Brogden, J., & Kitzmiller, D. (2016). Multi-
863	Radar Multi-Sensor (MRMS) Quantitative Precipitation Estimation: Initial Operating
864	Capabilities. Bulletin of the American Meteorological Society, 97(4), 621–638.
865	https://doi.org/10.1175/BAMS-D-14-00174.1
866	Zhang, J., Howard, K., Langston, C., Vasiloff, S., Kaney, B., Arthur, A., Cooten, S. V., Kelleher
867	K., Kitzmiller, D., Ding, F., Seo, DJ., Wells, E., & Dempsey, C. (2011). National
868	Mosaic and Multi-sensor QPE (NMQ) system. 18.
869	Zhang, S., & Pan, B. (2014). An urban storm-inundation simulation method based on GIS.
870	Journal of Hydrology, 517, 260–268. https://doi.org/10.1016/j.jhydrol.2014.05.044
871	Zhang, Z., Koren, V., Reed, S., Smith, M., Zhang, Y., Moreda, F., & Cosgrove, B. (2012). SAC-
872	SMA a priori parameter differences and their impact on distributed hydrologic model
873	simulations. Journal of Hydrology, 420–421, 216–227.
874	https://doi.org/10.1016/j.jhydrol.2011.12.004
875	
876	

Table Captions

radar derived estimates.

877

887

893

894

895

- Table 1. Description of the main components of the SWMM hydrologic-hydraulic model.
- Table 2. Parameter values of the Green-Ampt infiltration scheme adopted in SWMM.
- Table 3. Imperviousness and ground slope values assigned to the subcatchments, summarized as range of values for percentages of the basin area.
- Table 4. Summary of storm characteristics, including: start and end date and time in UTC, identified as the times when (i) any of the gage and radar products started measuring nonzero rainfall in the basin and (ii) all measured zero rainfall, respectively; type as defined by Dr. Larry Hopper from NWS (2020; personal communication); duration; rainfall totals observed by gages (R_g) ; and original (R_r^*) and bias corrected (in parentheses; R_r) mean areal rainfall totals of the
- Table 5. Parameters of the mixture of three gamma distributions used to characterize the distribution of errors: $f(e; w_1, \alpha_1, \beta_1, w_2, \alpha_2, \beta_2, w_3, \alpha_3, \beta_3) = \sum_{j=1}^3 w_j \cdot g(e; \alpha_j, \beta_j)$, where $g(e; \alpha_j, \beta_j)$ is the probability density function of the *j*-th gamma distribution of the errors, e (for simplicity, we dropped the dependence on R_r). Parameters values are reported for cluster 1 (C1) and 2 (C2).
 - **Table 6.** Quantification of uncertainty of simulated rainfall and runoff via skewness and *RIQR* of the ensemble rainfall and discharge at the basin outlet (in parentheses) averaged across each event duration (i.e., skewness and *RIQR* are computed for each time step and then averaged in time). Values are reported for each radar product.

Component	Description
Rain gages	Point measurements of rainfall over the duration of the modeling period
	from an actual rain gage or a radar pixel. Each sub-catchment is assigned
	rainfall from the closest gage or radar pixel center.
Sub-catchments	Hydrologic units of land delineated based on the local topography.
Conduits	Pipes or channels through which water is transported. This includes
	culverts and underground storm pipes.
Junctions	Drainage nodes that connect conduits to each other. Culvert inlets and
	outlets, pipe inlets and outlets, and manholes are all modeled as junctions.
	Junction properties include rim (surface) and invert (conduit base)
	elevations.
Outfall nodes	Drainage nodes at the downstream boundary of the catchment.
Storage units	Drainage nodes with an associated storage volume available.

 Table 1. Description of the main components of the SWMM hydrologic-hydraulic model.

Soil types	Percent of basin area	Suction head (cm)	Conductivity (cm/hr)	Initial Deficit
Avondale clay loam	1.2	38.53	0.15	0.21
Estrella loam	0.3	38.02	0.43	0.14
Gilman loam 1 to 3 percent slope	15.2	43.03	0.30	0.15
Glenbar clay loam	40.2	53.87	0.15	0.19
Laveen loam, 0 to 1 percent slope	34.4	36.50	0.61	0.11
Mohall clay loam	8.7	42.24	0.18	0.19

 Table 2. Parameter values of the Green-Ampt infiltration scheme adopted in SWMM.

Imperviousness (%)	Percent of basin area
0–50	7.8
51–60	10.0
61–70	19.6
71–80	35.1
81–100	27.5

Ground slope (%)	Percent of basin area
0–5	16.5
6–10	75.2
11-65	8.3

Table 3. Imperviousness and ground slope values assigned to the subcatchments, summarized as range of values for percentages of the basin area.

Start date	End date	Туре	Duration (h)	Gage (mm)	Stage IV (mm)	MRMS (mm)	GCMRMS (mm)
7/24/17	7/24/17	Monsoon	18	7.0	7.0	13.1	15.7
2:00	20:00		10	7.0	(8.9)	(8.6)	(11.4)
7/31/18	7/31/18	Monsoon	6	5.0	5.8	20.0	11.0
3:00	9:00		O	3.0	(7.4)	(13.1)	(8.3)
10/7/18	10/7/18	Transition	11	10.0	10.0	17.1	7.1
8:00	19:00		11	10.0	(12.6)	(11.2)	(5.3)
9/23/19	9/24/19	Tropical/	22	6.0	6.8	15.8	8.6
10:00	19:00	Transition	33	6.0	(8.7)	(10.4)	(6.5)

Table 4. Summary of storm characteristics, including: start and end date and time in UTC, identified as the times when (i) any of the gage and radar products started measuring nonzero rainfall in the basin and (ii) all measured zero rainfall, respectively; type as defined by Dr. Larry Hopper from NWS (2020; personal communication); duration; rainfall totals observed by gages (R_g); and original (R_r^*) and bias corrected (in parentheses; R_r) mean areal rainfall totals of the radar derived estimates.

Parameter	Stage IV		MRMS		GCMRMS	
	C1	C2	C1	C2	C1	C2
α_{I}	1.34	6.50	2.89	5.16	1.55	1.76
α_2	55.34	1.26	13.58	1.09	11.75	19.93
α_3	19.97	357.00	6.50	9.18	35.85	38.16
eta_{I}	0.95	0.14	0.29	0.14	0.72	0.60
β_2	0.01	1.08	0.17	1.10	0.07	0.04
β_3	0.05	0.002	0.55	0.21	0.04	0.04
WI	0.47	0.46	0.92	0.64	0.47	0.61
W2	0.37	0.33	0.05	0.23	0.43	0.31
W3	0.16	0.21	0.03	0.13	0.10	0.08

Table 5. Parameters of the mixture of three gamma distributions used to characterize the distribution of errors: $f(e; w_1, \alpha_1, \beta_1, w_2, \alpha_2, \beta_2, w_3, \alpha_3, \beta_3) = \sum_{j=1}^3 w_j \cdot g(e; \alpha_j, \beta_j)$, where $g(e; \alpha_j, \beta_j)$ is the probability density function of the *j*-th gamma distribution of the errors, e (for simplicity, we dropped the dependence on R_r). Parameters values are reported for cluster 1 (C1) and 2 (C2).

Storm start date	Stage IV	MRMS	GCMRMS	Stage IV	MRMS	GCMRMS
		Skewness	(-)		RIQR (%	6)
			Rainfall (Discha	arge at the outlet)		
7/24/17	3.2	1.7	1.4	71.0	68.4	59.5
//24/1/	(2.0)	(1.1)	(0.4)	(66.9)	(51.6)	(22.4)
7/21/10	2.9	1.5	1.5	70.1	68.2	69.2
7/31/18	(0.8)	(1.0)	(0.9)	(45.0)	(43.7)	(41.1)
10/7/10	2.1	1.7	1.0	59.7	67.9	41.5
10/7/18	(0.9)	(1.3)	(0.5)	(55.8)	(49.0)	(27.4)
0/22/10	2.6	1.7	1.3	74.6	70.2	56.1
9/23/19	(2.5)	(0.9)	(0.5)	(47.0)	(78.0)	(50.3)

Table 6. Quantification of uncertainty of simulated rainfall and runoff via skewness and *RIQR* of the ensemble rainfall and discharge at the basin outlet (in parentheses) averaged across each event duration (i.e., skewness and *RIQR* are computed for each time step and then averaged in time). Values are reported for each radar product.

Figure Captions

922923

924

925

926

927

928

929

930

931

932

933

934

935

936

937

938

939

940

941

942

943

944

Figure 1. (a) Metropolitan area of Phoenix, AZ along with location of KIWA WSR-88D weather radar, study basin, and rain gages of the Flood Control District of the Maricopa County (FCDMC) network in Maricopa and Pinal Counties, displayed with two different colors depending on the distance from the radar (labelled as cluster 1 and 2). (b) Boundaries of the study catchment and subcatchments in downtown Phoenix (near the corner of W Roosevelt St and S 7th Ave), along with outlet, underground conduits of the stormwater infrastructure system, grids of Stage IV and MRMS (same as GCMRMS) radar products, and rain gage of the FCDMC network. Figure 2. Flooding in the study catchment at Central Ave and Washington Street in Phoenix, AZ during the storm on September 23, 2019. **Figure 3**. Scatterplots of radar rainfall estimates, R_r , and true rainfall approximated by the gage estimates, R_g , for cluster 2. A total of 8,645, 8,859, and 8,605 non-zero pairs for (a) Stage IV, (b) MRMS, and (c) GCMRMS are shown using different colors based of their relative frequency. In each panel, the dashed red line is the systematic component estimated with the Epanechnikov kernel, and the solid black line is the power law of equation (5). Parameters of the power law are a = 1.12, b = 0.90 for Stage IV; a = 1.37, b = 0.77 for MRMS; and a = 1.86, b = 0.66 for GCMRMS. **Figure 4.** Relations between $e(R_r)$ and R_r for the different radar products, along with quantiles of the empirical (dotted lines) and mixed gamma (solid lines) distributions for cluster 2. **Figure 5.** Comparison of survival functions of the empirical distribution and mixture of three gamma distributions for cluster 2.

Figure 6. Time series of rainfall recorded at the gage (R_g) , basin mean areal rainfall estimated by the three radar products (R_r^*) , and boxplots of the N = 100 Monte Carlo simulations of the radar rainfall error model for the four events of Table 2. Boxes and whiskers of the boxplots show the 50% and 90% confidence intervals, respectively, while the horizontal line is the median. Times are in UTC. **Figure 7.** Hydrographs simulated by the SWMM model at the pipe located at the catchment outlet under rainfall recorded at the gage (R_g) , original radar QPEs (R_r^*) , and an ensemble of rainfall fields generated with the error model. The corresponding N = 100 outflow simulations are plotted with shaded areas showing the 50% (light gray) and 90% (dark gray) confidence intervals, while the black line is the median. Figure 8. Flood metrics simulated by 1D SWMM for the selected storms with rainfall recorded at the gage (R_g) , original radar QPEs (R_r^*) , and ensemble of rainfall fields generated with the error model plotted through boxplots (boxes and whiskers show the 50% and 90% confidence intervals, respectively). See text for definition of the flood metrics. tmax is measured in hours since the simulations starts. Figure 9. Uncertainty of flood extent maps for the storm on July 31, 2018 simulated by PCSWMM under (a)-(c) Stage IV, (d)-(f) MRMS, and (g)-(i) GCMRMS products.

Figure 10. As Fig. 9 but for the storm on October 7, 2018.

945

946

947

948

949

950

951

952

953

954

955

956

957

958

959

960

961

962

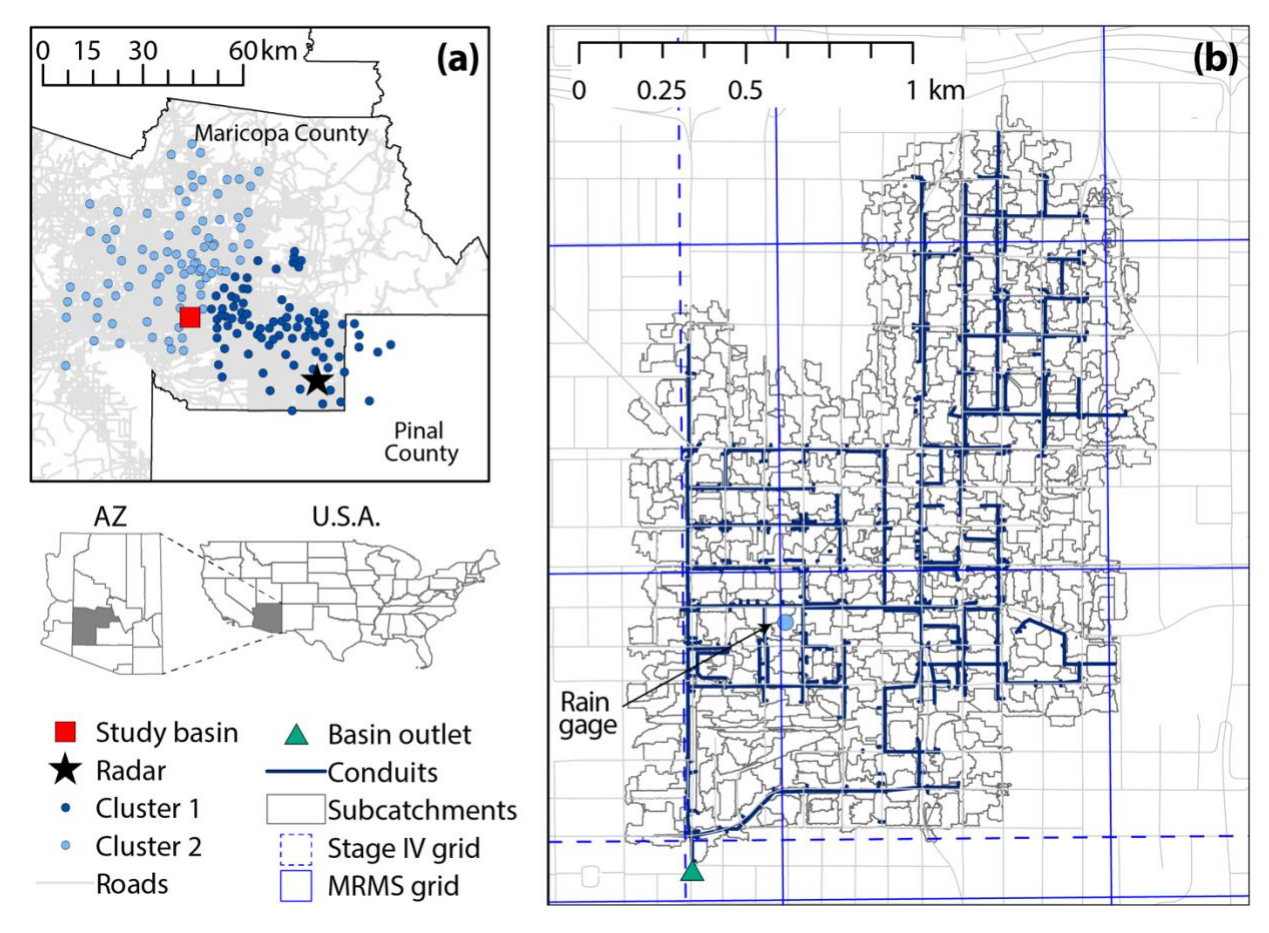


Figure 1. (a) Metropolitan area of Phoenix, AZ along with location of KIWA WSR-88D weather radar, study basin, and rain gages of the Flood Control District of the Maricopa County (FCDMC) network in Maricopa and Pinal Counties, displayed with two different colors depending on the distance from the radar (labelled as cluster 1 and 2). (b) Boundaries of the study catchment and subcatchments in downtown Phoenix (near the corner of W Roosevelt St and S 7th Ave), along with outlet, underground conduits of the stormwater infrastructure system, grids of Stage IV and MRMS (same as GCMRMS) radar products, and rain gage of the FCDMC network.



Figure 2. Flooding in the study catchment at Central Ave and Washington Street in Phoenix, AZ during the storm on September 23, 2019.

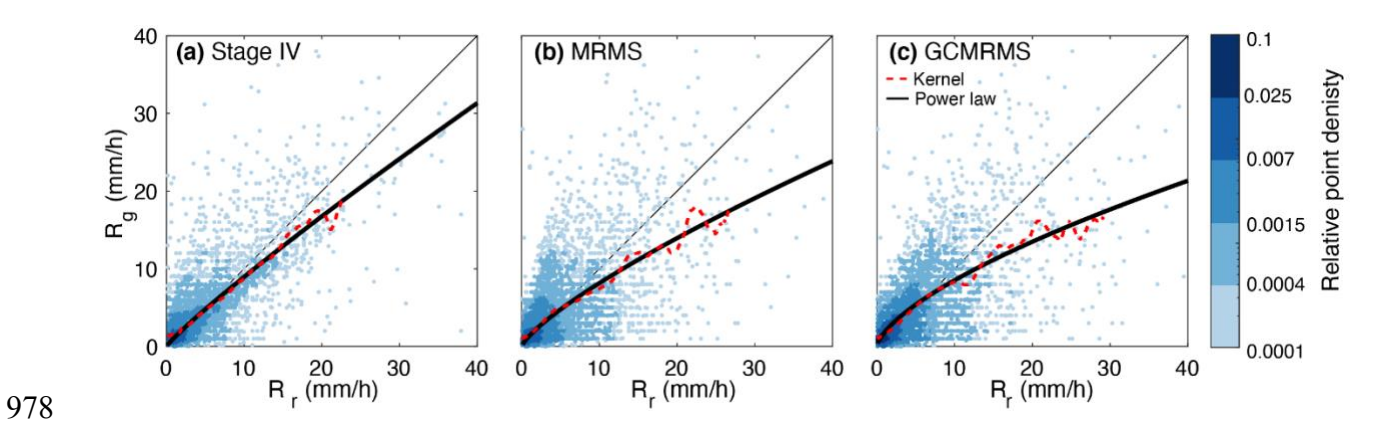


Figure 3. Scatterplots of radar rainfall estimates, R_r , and true rainfall approximated by the gage estimates, R_g , for cluster 2. A total of 8,645, 8,859, and 8,605 non-zero pairs for (a) Stage IV, (b) MRMS, and (c) GCMRMS are shown using different colors based of their relative frequency. In each panel, the dashed red line is the systematic component estimated with the Epanechnikov kernel, and the solid black line is the power law of equation (5). Parameters of the power law are a = 1.12, b = 0.90 for Stage IV; a = 1.37, b = 0.77 for MRMS; and a = 1.86, b = 0.66 for GCMRMS.

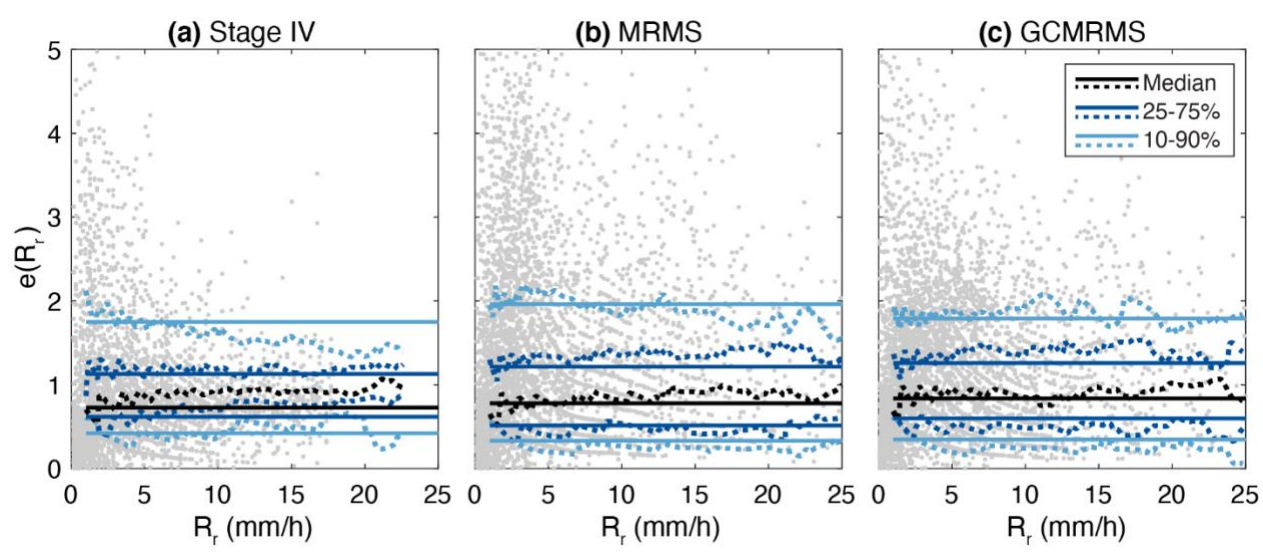


Figure 4. Relations between $e(R_r)$ and R_r for the different radar products, along with quantiles of the empirical (dotted lines) and mixed gamma (solid lines) distributions for cluster 2.

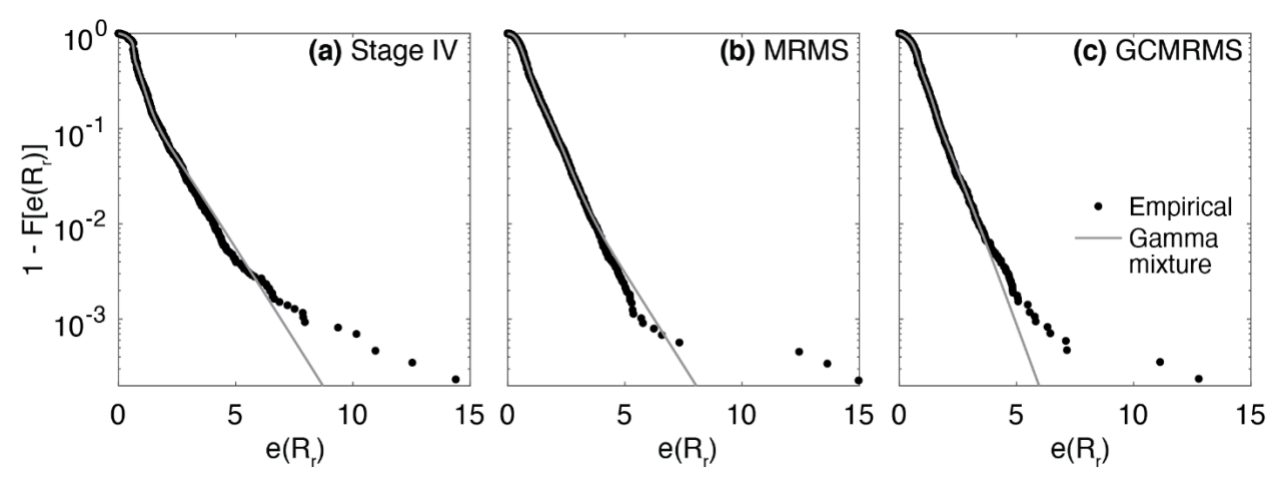


Figure 5. Comparison of survival functions of the empirical distribution and mixture of three gamma distributions for cluster 2.

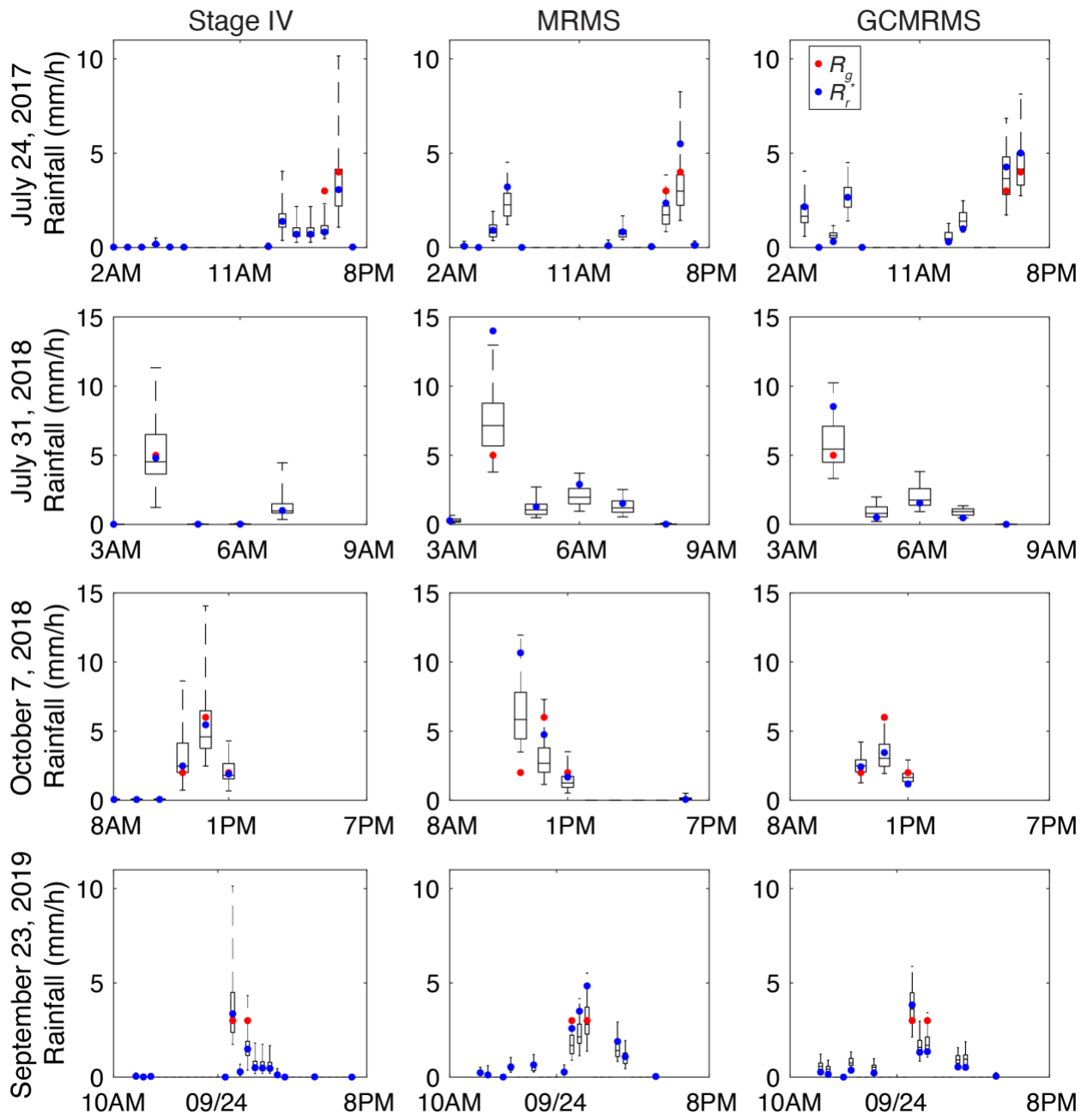


Figure 6. Time series of rainfall recorded at the gage (R_g) , basin mean areal rainfall estimated by the three radar products (R_r^*) , and boxplots of the N = 100 Monte Carlo simulations of the radar rainfall error model for the four events of Table 2. Boxes and whiskers of the boxplots show the 50% and 90% confidence intervals, respectively, while the horizontal line is the median. Times are in UTC.

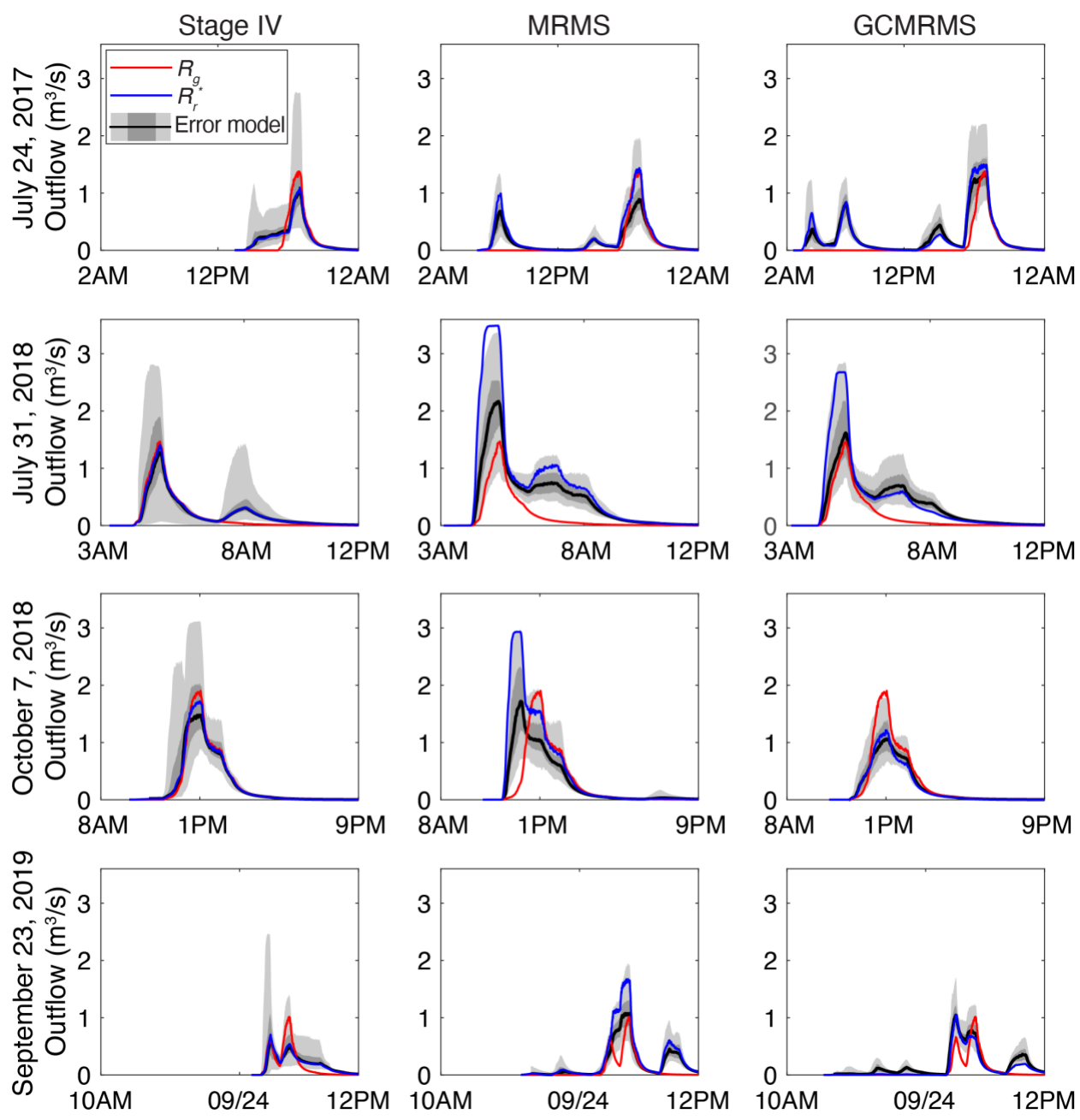


Figure 7. Hydrographs simulated by the SWMM model at the pipe located at the catchment outlet under rainfall recorded at the gage (R_g) , original radar QPEs (R_r^*) , and an ensemble of rainfall fields generated with the error model. The corresponding N = 100 outflow simulations are plotted with shaded areas showing the 50% (light gray) and 90% (dark gray) confidence intervals, while the black line is the median.

 $\frac{1001}{1002}$

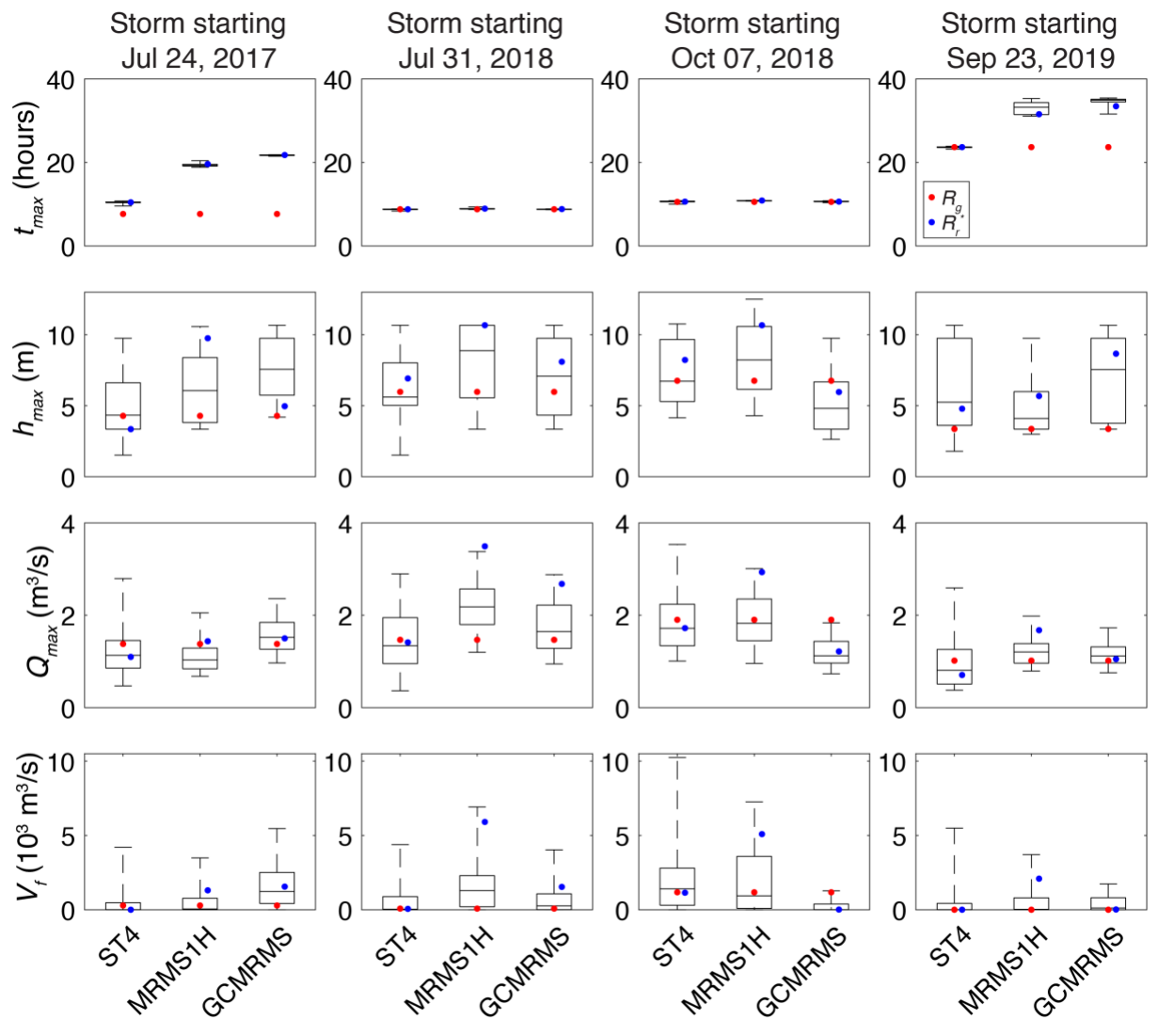


Figure 8. Flood metrics simulated by 1D SWMM for the selected storms with rainfall recorded at the gage (R_g), original radar QPEs (R_r^*), and ensemble of rainfall fields generated with the error model plotted through boxplots (boxes and whiskers show the 50% and 90% confidence intervals, respectively). See text for definition of the flood metrics. t_{max} is measured in hours since the simulations starts.

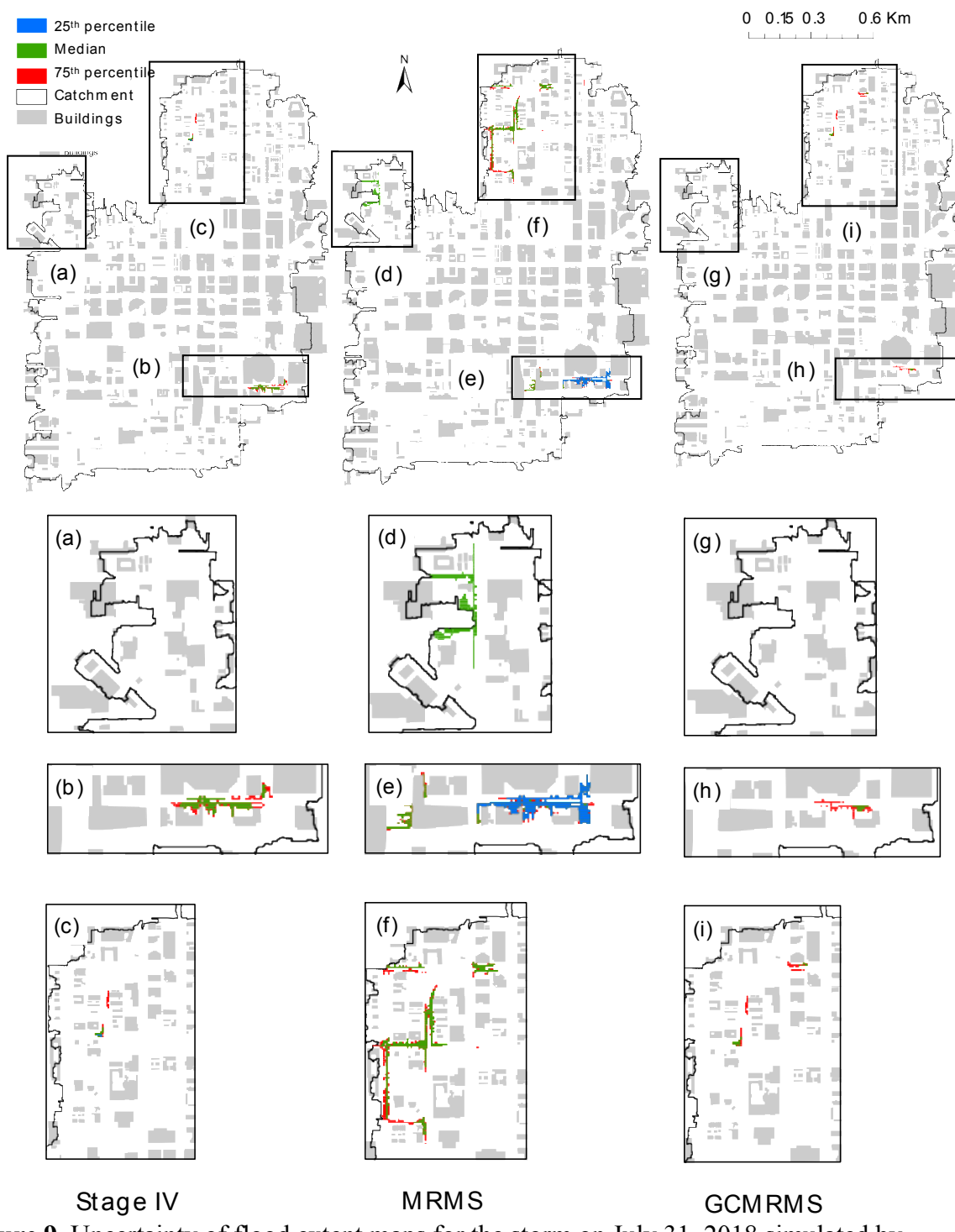


Figure 9. Uncertainty of flood extent maps for the storm on July 31, 2018 simulated by PCSWMM under (a)-(c) Stage IV, (d)-(f) MRMS, and (g)-(i) GCMRMS products.

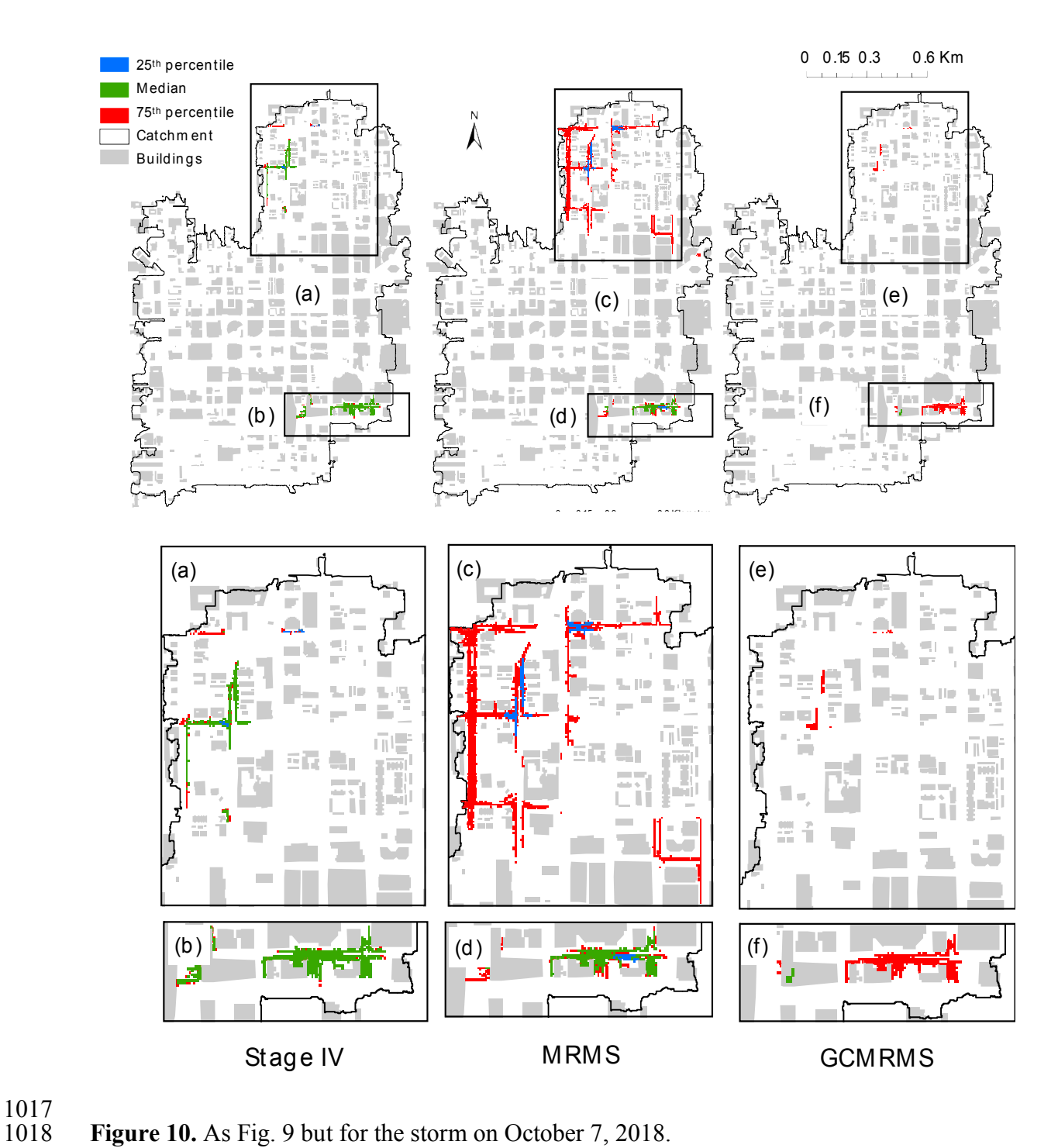


Figure 10. As Fig. 9 but for the storm on October 7, 2018.